Elastic Response of Porous Matrix Plain Weave Fabric Composites: Part I—Modeling

J. L. KUHN AND P. G. CHARALAMBIDES
Department of Mechanical Engineering
The University of Maryland
1000 Hilltop Circle
Baltimore, MD 21228

(Received March 5, 1997)
(Revised August 26, 1997)

ABSTRACT: In this first of a two-part series of papers, improved two-dimensional modified lamination theory and three dimensional finite element models are developed for the elastic analysis of plain weave fabric composites. New more accurate surface functions are proposed to model the geometry of the woven unit-cell. These geometry functions are implemented in both the analytical and finite element models which allows for direct model comparison. These models take into account the effects of the complex microstructure exhibited by both Chemical Vapor Infiltrated (CVI) woven ceramic matrix composites and traditional woven polymer matrix composites. The spatially dependent directional orthotropy of the fiber bundles is incorporated in both the analytical and numerical 3-D finite element models. In addition to the interbundle matrix porosity, the models also account for the presence of porosity within the bundles, as well as the presence of thin fiber and bundle coatings. The models are developed in a general manner such that they can be used to assess the effective elastic response of both *stiff*-ceramic and *soft*-polymer matrix woven composites. Case studies of pure remote tension and shear are formulated, and the theoretical platform required for the analytical and numerical evaluation of the in-plane effective elastic properties of *stiff*-ceramic and *soft*-polymer matrix woven composites is presented. Extensive parameter studies, discussion of the results and overall conclusions are reported in the accompanied manuscript with the title extension, Part II–Results. This work extends and refines previous micromechanical models aimed at predicting the macromechanical response of woven composite systems. It also establishes for the first time a hierarchical modeling framework, which is needed in the modeling of the effects of complex microstructures often exhibited by *soft*-polymer and *stiff*-ceramic porous matrix woven composites.

KEY WORDS: elastic, micromechanics, effective, properties, plain weave, composites, fiber, bundles, unit-cell, finite elements, porosity, coating, volume fraction.

0021-9983/98/16 1426–46 $10.00/0

1. INTRODUCTION

POLYMER MATRIX WOVEN fabric composites have gained relatively widespread application due to a number of advantages over unidirectional composites. Woven fabric composites offer more balanced directional properties, enhanced impact resistance, increased out-of-plane strength and stiffness, and improved ease of handling and quality control at reduced net cost. However, the above gains are somewhat offset by the concurrent reduction of the composite in-plane properties. In addition, the woven systems exhibit a rather complex mechanical response during loading and resulting failure. For example, under remotely applied uniaxial tensile loading, non-uniform stresses and strains develop as a result of both the woven microstructure and material heterogeneities. The non-planar woven bundles, when stretched, encounter resistance by the surrounding matrix material and as a result give rise to normal and shear interface stresses along the bundle/matrix boundary. The stretching of the bundles under uniaxial loading is also resisted by the bending stiffness of the bundle itself which gives rise to micro-bending stresses and strain within the fiber bundle. These rather intricate stress inducing mechanisms are further complicated by multi-directional effects in 2-D and 3-D woven systems. The initiation of damage and ultimate fracture of such woven systems has also been shown to be complex and as such, difficult to model and predict. As observed by various researchers (Zok et al. [1], Steyer and Zok [2], McNulty and Zok [3], and Bordia et al. [4,5]), ceramic matrix woven composites may undergo extensive damage due to bundle transverse and longitudinal matrix cracking, bundle/matrix delamination, matrix cracking, fiber pull-out and possibly other energy dissipating mechanisms. As a result, the overall non-linear response of ceramic matrix woven systems is fairly difficult to predict, due to the intricate interlink between the design of the microstructure which includes the material selection, bonding characteristics, and system processing to the active modes of failure that may control the ultimate failure of the woven system under a multi-axial state of stress.

Over the last decade researchers have developed analytical and numerical models [6–20] that utilize certain micro-structural parameters to aid in the selection of the optimal woven structure for a given application. Until recently [20], efforts were focused on polymer matrix woven fabric composites which are mostly used in low temperature applications. New Chemical Vapor Infiltration (CVI) technologies have recently been successfully used in the fabrication of woven ceramic matrix composites (CMC's). These systems are typically manufactured by first interlacing bundles of loose fibers to form a woven mat. In order to control the fiber/matrix interfacial properties, a low modulus coating may often be applied around the fiber reinforcements before the matrix is introduced via CVI techniques. Such CVI ceramic matrix woven composites produced by DuPont and tested for strength, stiffness, and toughness [1–5] were shown to exhibit additional

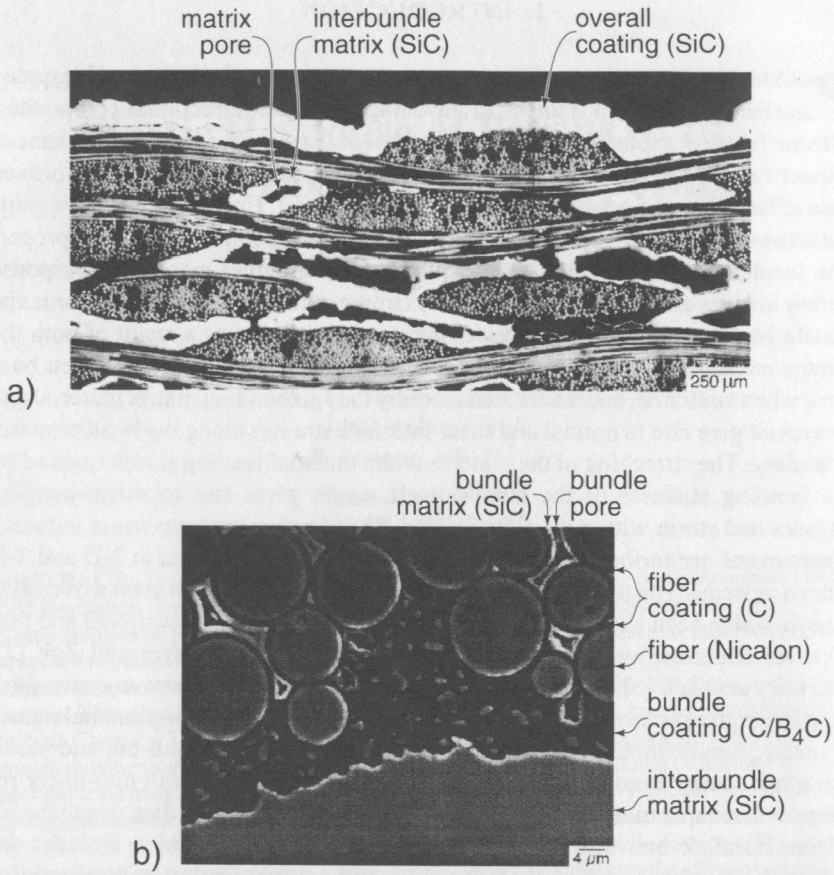

Figure 1. *Micrographs of a CVI ceramic matrix woven composite provided by Zok et al. [1]. (a) A composite laminate comprised of several randomly stacked woven plies. (b) An enlarged view of a region along the edge of a fiber bundle.*

micro-structural characteristics, such as a soft discontinuous bundle coating, appreciably large matrix voids between weaves, distributed porosity within bundles and an overall protective coating placed over the woven laminate aiming at oxidation of the interior. A typical cross section of the DuPont woven system is shown in the micrographs in Figures 1(a) and 1(b), which were obtained by Zok et al. [1]. In Figure 1(a), the macroscopic cross section is characterized by bundles of fibers woven normal and parallel to the plane of the cross section, large voids in the matrix between fiber bundles, and an external coating visible along the top of the cross section. The fiber bundles shown in Figure 1 are comprised of a brittle fiber

coated with a compliant phase, and surrounded by a porous brittle matrix. The solid region along the bottom of the image is the interbundle matrix, and the dark material between the fibrous region and the interbundle matrix is the compliant bundle coating.

As mentioned previously, much work has been done to model the linear behavior of woven PMC's which by comparison to the DuPont system shown in Figure 1 exhibit a more regular but yet complex microstructure. Ishikawa and Chou [6–10] developed analytical models using the classical laminate theory for infinitesimal columns within a simplified 1-D woven unit-cell. Ishikawa et al. [11] reported experimental studies which utilized the Ishikawa and Chou [6–10] models. Naik and Shembekar [12] presented a model based on the classical laminate theory, with a geometry model based on that of Chou and Ishikawa [10], and addressed the 2-D nature of the woven structure. The latter models were improved by Naik and Shembekar [12] to account for the 2-D geometry effects. In their studies, Naik and Shembekar also presented improved methods of property averaging, and took into account the microstructure of the tows using a Composite Cylinder Assemblage (CCA) model. Raju and Wang [14] presented models similar to that of Naik and Shembekar for plain weave, five-, and eight-harness satin weave composites, using a more approximate approach to property averaging and without taking into account the microstructure of the tows.

The aforementioned analytical approaches are based on the classical laminate theory and, as such, yield engineering approximations of the effective properties. Shkoller and Hegemier [15] performed rigorous mathematical homogenization of the unit-cell, and Dasgupta and Bhandarkar [16] combined homogenization theory and finite element analysis using certain simplifying assumptions. Due to the complex geometry of the woven unit-cell, both Shkoller and Hegemier [15] and Dasgupta and Bhandarkar [16] obtained the effective properties of the woven unit-cell via the finite element method. While the accuracy of these studies yielded improved results for the effective mechanical response of the woven system, they were rather involved and rendered themselves somewhat impractical for design applications. Zhang and Harding [17] used an energy equivalence method and finite element analysis to determine the approximate effective properties of a one-direction undulation model, much like the fiber undulation model of Ishikawa and Chou [9]. Whitcomb [18] presented a three-dimensional finite element model to determine the microstresses and effective elastic properties of a plain weave composite. Whitcomb also used an energy equivalence method in conjunction with the use of an average stress and strain in determining the effective woven unit-cell properties. More recently, Naik [21–23] employed a 3-D stiffness averaging approach based on an iso-strain assumption to model the effective linear and nonlinear response of polymer matrix composites with various fabric architectures.

While all of the above work has pertained to woven PMC's, in recent years some research has been reported on woven CMC's. A large number of experimental

studies are, for example, included in the *Ceramic Engineering and Science Proceedings* [24–34]. In other studies, Vaidyanathan, Kelkar and Sankar [19] applied the classical lamination theory to predict the elastic properties of plain weave SiC/SiC composite. Kuo and Chou [20] introduced a mechanics of materials fiber bundle model for woven CMC's which represents a simplification over the classical laminate theory models. Kuo and Chou [20] also incorporated in their model the effects of transverse cracking to capture some of the non-linear damage characteristics associated with the fracture of woven brittle matrix composites.

The development of most of the aforementioned woven composite models was made possible by making use of several simplifying assumptions on the woven microstructure. For example, most of the models account for only two constituents, i.e., the fiber and the matrix where the fiber directional effects are introduced via the effective bundle properties. In addition, most of the existing models on woven composites utilize discontinuous approximate geometry functions in representing the complex woven micro-structural architecture. Although the model by Chou and Ishikawa [10] accounts to a certain degree for the tow (or bundle) microstructure, neither that model nor any other model currently available can concurrently account for the effects of microconstituents such as the fiber coating, the bundle coating, bundle matrix porosity and the presence of large interbundle matrix voids as those exhibited by the DuPont system shown in Figure 1 which is more typical of CVI woven ceramic matrix composites.

In this work, we propose a fundamental micromechanics model that can be used to predict the effective elastic response of CVI ceramic matrix composites exhibiting complex microstructures such as that shown in Figure 1. As discussed later in the paper, the proposed model accounts in a general sense for the presence of microconstituents such as multiple bundle coating layers, coating applied over the fiber bundle reinforcements, bundle matrix porosity and the presence of dispersed porosity and large voids within the interbundle matrix phase. Thus, within the linear elastic regime, the influence of the above micro-structural characteristics on the elastic effective properties of woven systems can be studied via the proposed model for both PMC and CMC woven systems. The model developed herein, utilizes a new family of geometry functions associated with the bundle/matrix interface. These functions are continuous and piecewise smooth throughout the domain of the unit-cell, and are given by a single, more manageable expression for each surface. Through these functions, the effects of bundle geometry pertaining to its height/width ratio and to its interbundle space width on the overall woven system response are examined. The model incorporates the fundamental features of existing models [6–20], and utilizes a 2-D modified lamination theory approach similar to that used by Naik and Shembekar [12] and Naik and Ganesh [13]. In addition to the analytical approximate model, in this work we report on parallel 3-D finite element studies which were performed over a reference unit-cell with micro-structural characteristics similar to those used in the analytical studies. In

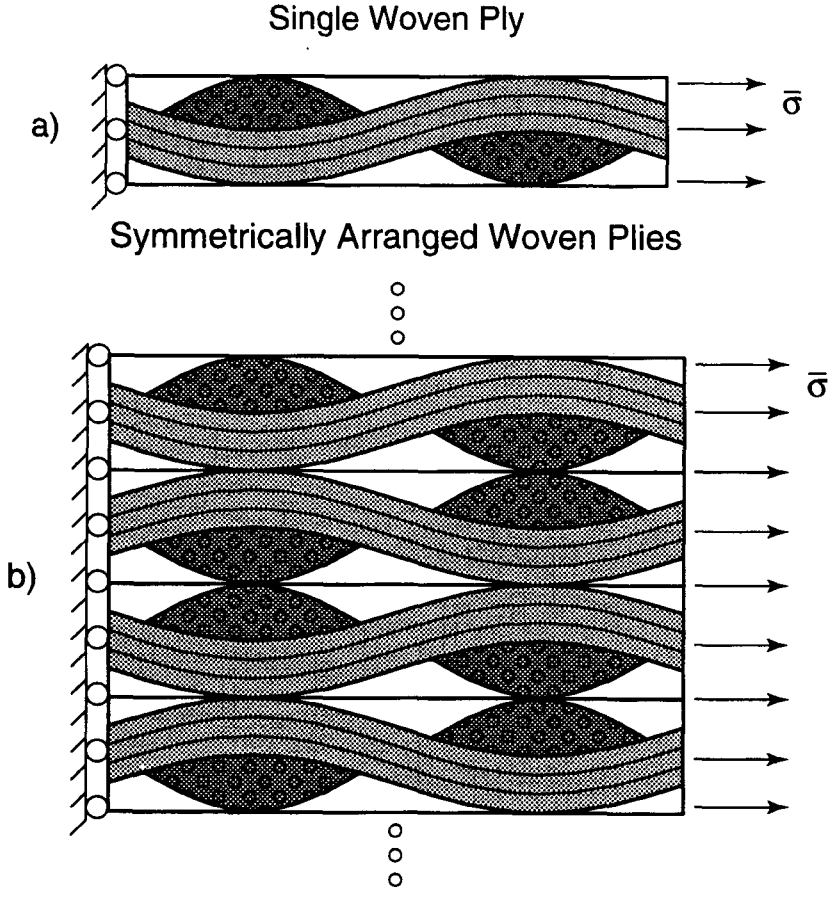

Figure 2. *(a) A single woven ply subjected to remote tension loading. (b) A repeating sequence of woven plies stacked with alternating symmetry under remote tension.*

the second part of this study, which is presented in the accompanying paper, the numerical results are compared to the analytical prediction through extensive parameter studies and are used to evaluate the elastic response of a single woven ply [see Figure 2(a)] versus an infinite sequence of woven plies stacked with alternating symmetry as shown in Figure 2(b). The elastic response of the above two cases, can be used to establish upper and lower bound estimates for the elastic response of a woven system comprised of a finite number of randomly stacked plies. In the second part of this manuscript, selective finite element microstresses and microstrains are reported as needed to asses the effects of local micro-bending during tension as observed experimentally by Zok et al. [1], Steyer and Zok [2], and

McNulty and Zok [3] who conducted tensile experiments using the DuPont woven CVI system.

2. ANALYTICAL MODELING

The woven composites considered herein consist of untwisted fiber bundles woven together at right angles in the plane of the composite plate as shown in Figure 3. The fiber bundles are called tows when considered as a single structure. The tows in the longitudinal direction are called warp tows and those in the transverse direction are called fill tows. The tows may be woven together in a number of dif-

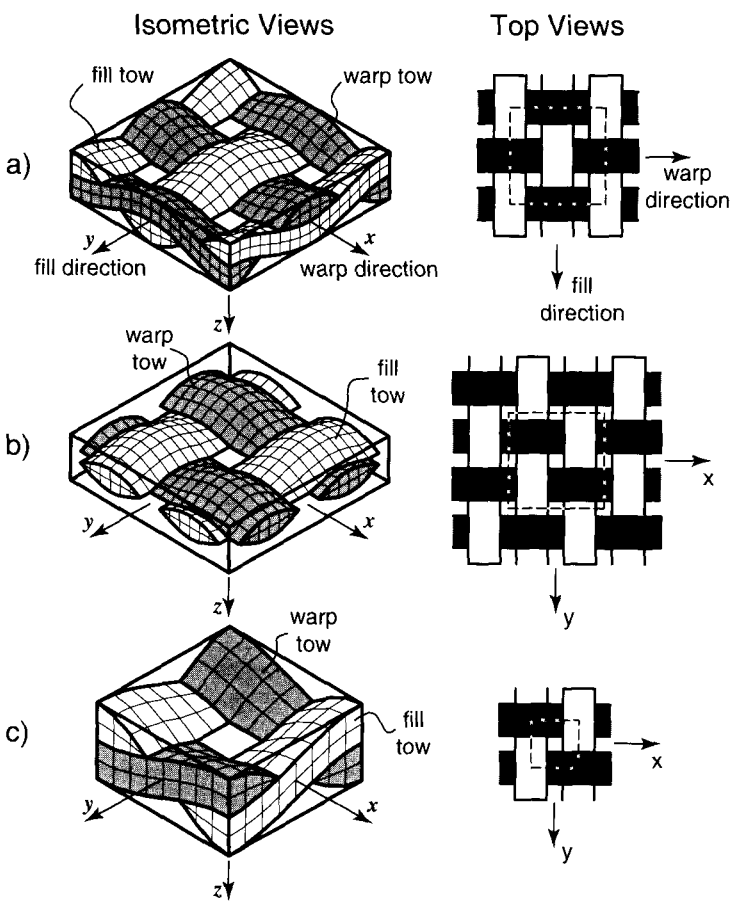

Figure 3. *The three unit-cells of the plain weave fabric composite. (a) Full repeating and geometrically symmetric unit-cell. (b) Repeating unit-cell. (c) Symmetric unit-cell.*

ferent patterns, the simplest of which is the plain weave shown in Figure 3. The fill and warp tows may also be composed of different material systems, in which case the composite is termed a hybrid composite. The composite structure treated in this paper is a non-hybrid two-dimensional plain weave fabric.

Three plain weave unit-cells are shown in Figure 3. As shown in the figure, on the left are isometric views and on the right are top views for each unit-cell considered. The elastic mechanical response of the woven system represented through the full unit-cell shown in Figure 3(a) may be modeled by applying appropriate symmetry conditions to the third and simplest unit-cell shown in Figure 3(c). Any of these unit-cells may be used, however, the boundary conditions along the out-of-plane faces of the repeating unit-cell are not clearly defined. Only the symmetric unit-cell was used in the development of both the analytical and 3-D finite element models herein.

2.1 Unit-Cell Model Geometry

Here we present a completely new woven unit-cell model (see Figures 4, 5, and 6) which encompasses both repeating and symmetric cells of a plain weave fabric, and allows for refined description of the actual woven system geometry. This model, for example, takes into account the matrix filled space between tows and the undulation of the fibers in both directions, and also allows for variation in the cross sections of the warp and fill tows. The model also takes into account the continuity of the fiber bundles in both the fill and warp directions, and the non-symmetrical cross section of the tows. Note that the fiber orientation within the bundles varies continuously as a function of x and y for the warp and fill tows respectively. For direct comparison purposes the analytical and numerical finite element models presented in this work are developed using the same unit-cell geometry. The model is named the Plain Weave Bi-Directional Undulation (PW-BDU) model to be consistent with the nomenclature of Ishikawa and Chou [7]. The PW-BDU unit-cell geometry model developed herein utilizes the five geometry parameters shown schematically in Figure 4(a).

An accurate description of the spatial function defining the bundle/matrix 3-D interface and thus the 3-D shape and location of the bundles within the reference domain of a woven unit-cell is required for the development of the unit-cell model geometry. In other published studies, a good number of unit-cell geometry models have been introduced by various authors. Some of these models are based on a rather crude approximation of the actual woven system geometry whereas other models are rather complex and cumbersome to implement. Possibly due to the above reasons the existing analytical and finite element models do not make use of the same woven-cell goemetry functions which renders difficult the direct comparison between the analytical and numerical predictions of the woven mechanical response.

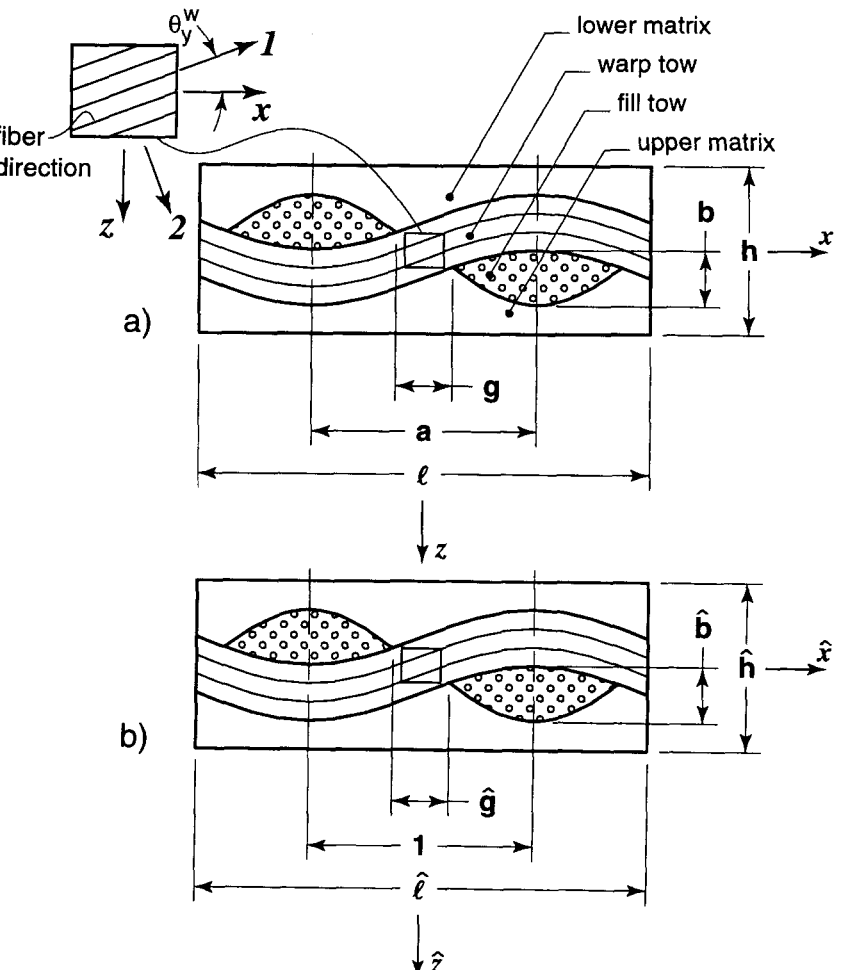

Figure 4. *(a) Cross-sectional geometry and parameters of the plain weave bi-directional undulation model. (b) The non-dimensional woven cross section.*

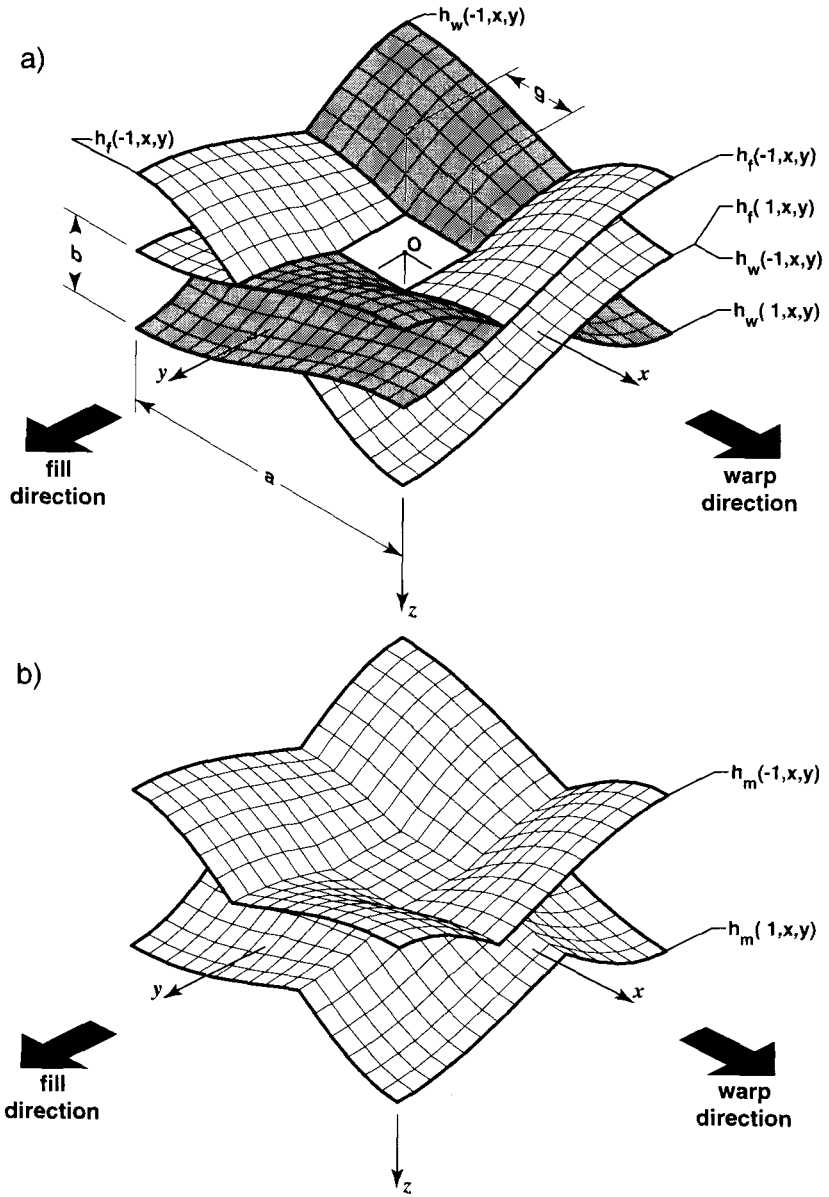

Figure 5. *Top and bottom surface functions of (a) the tows and (b) the matrix of the symmetric unit-cell corresponding with Equations (1), (2), and (6).*

$$H(x) = \begin{cases} 0 & x < 0 \\ 1 & 0 \le x \end{cases}$$

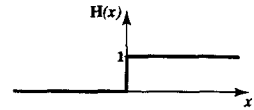

$$\operatorname{sign}(x) = \frac{x}{|x|}$$

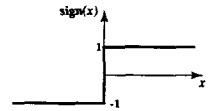

$$R(\hat{x}) = \begin{cases} \frac{\hat{x}}{\hat{g}} + \frac{1}{2} & |\hat{x}| < \frac{\hat{g}}{2} \\ H(\hat{x}) & \frac{\hat{g}}{2} \le |\hat{x}| \le 1 - \frac{\hat{g}}{2} \\ \frac{(\operatorname{sign}(\hat{x}) - \hat{x})}{\hat{g}} + \frac{1}{2} & 1 - \frac{\hat{g}}{2} \le |\hat{x}| \le 1 + \frac{\hat{g}}{2} \end{cases}$$

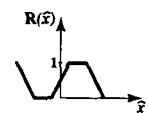

$$F_H(\hat{x}) = H(|\hat{x}| - \tfrac{\hat{g}}{2}) - H(|\hat{x}| + \tfrac{\hat{g}}{2} - 1)$$

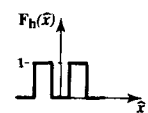

$$F_R(n, \hat{x}, \hat{y}) = R(n\operatorname{sign}(\hat{y})\hat{x})$$

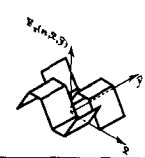

Figure 6. *The auxiliary functions and their representative profiles used in constructing the geometry surface functions.*

In accordance with Figure 4(a), l represents the length of the unit-cell, h represents the height of the woven ply, a denotes the half period of the unit-cell, whereas b and g are used to represent the bundle height and interbundle space width respectively.

2.1.1 BUNDLE/MATRIX INTERFACE SHAPE FUNCTIONS

The independent geometry parameters shown in Figure 4(a) were used to develop the bundle/matrix interface shape functions within the domain occupied by the woven unit-cell. A detailed formulation of the woven geometry shape functions is presented in Reference [35] where a sinusoidal shape is assumed for the undulating yarn paths. The cross sections of the tows are constructed from two different sinusoidal shapes for the top and bottom edges, allowing for non-symmetry and shape variations of the tow cross sections. In this model the area of the tow cross section and fiber volume fraction are assumed to remain constant along the

length of the tow. The surface shape functions employed herein are shown in Figure 5 and have the following non-dimensional form:

$$\hat{h}_w(n,\hat{x},\hat{y}) = \frac{\hat{b}}{2}F_H(\hat{y})\,\mathrm{sign}(\hat{y})\Big\{-\sin(\pi\hat{x}) + nF_R(n,\hat{x},\hat{y})\sin(\pi\hat{y}) + nF_R(-n,\hat{x},\hat{y})\left[(1+\beta)\sin\left(\frac{\pi(\hat{y}-\mathrm{sign}(\hat{y})\hat{g}/2)}{(1-\hat{g})}\right) - \mathrm{sign}(\hat{y})\beta\right]\Big\} \tag{1}$$

and

$$\hat{h}_f(n,\hat{x},\hat{y}) = -\hat{h}_w(-n,\hat{y},\hat{x})$$

$$n = 1 \Rightarrow \text{top surface} \tag{2}$$

$$n = -1 \Rightarrow \text{bottom surface}$$

where $\hat{h}_w$ and $\hat{h}_f$ are the non-dimensional surfaces of the warp and fill tows respectively, with $n = 1$ and $n = -1$ describing the top and bottom tow surfaces respectively. The above shape functions utilize the following auxiliary functions:

$$H(x) = \begin{cases} 0 & x < 0 \\ 1 & 0 \le x \end{cases}$$

$$\mathrm{sign}(x) = \frac{x}{|x|}$$

$$R(\hat{x}) = \begin{cases} \dfrac{\hat{x}}{\hat{g}} + \dfrac{1}{2} & |\hat{x}| < \dfrac{\hat{g}}{2} \\ H(\hat{x}) & \dfrac{\hat{g}}{2} \le |\hat{x}| \le 1 - \dfrac{\hat{g}}{2} \\ \dfrac{(\mathrm{sign}(\hat{x}) - \hat{x})}{\hat{g}} + \dfrac{1}{2} & 1 - \dfrac{\hat{g}}{2} \le |\hat{x}| \le 1 + \dfrac{\hat{g}}{2} \end{cases}$$

$$F_H(\hat{x}) = H\left(|\hat{x}| - \frac{\hat{g}}{2}\right) - H\left(|\hat{x}| + \frac{\hat{g}}{2} - 1\right)$$

$$F_R(n,\hat{x},\hat{y}) = R(n \text{ sign } (\hat{y})\hat{x})$$

and

$$\beta = \sin\left(\frac{\pi\hat{g}}{2}\right)$$

These functions are assembled in a manner such that the resulting surface equations are continuous. The profile of each auxiliary function is shown in Figure 6, and are cast in terms of the following non-dimensional parameters:

$$\hat{x} \equiv \frac{x}{a} \qquad \hat{b} \equiv \frac{b}{a} \qquad \hat{h}_f \equiv \frac{h_f}{a}$$
$$\hat{y} \equiv \frac{y}{a} \qquad \hat{g} \equiv \frac{g}{a} \qquad \hat{h}_w \equiv \frac{h_w}{a} \tag{3}$$

with a being the half period of the unit-cell shown in Figures 4 and 5. The orientation of the principal material directions of each of the tows with respect to the global coordinate system is specified by the angles of rotation about the appropriate global axis. All of the fibers in each section of the tows are assumed to be parallel to the centroid of the fiber bundle. The angles of rotation for the warp and fill tows are given as follows [θ_y^w is shown in Figure 4(a)]:

$$\theta_y^w = \text{atan}\left(\frac{\partial \hat{h}_w^c}{\partial \hat{x}}\right)$$
$$\theta_x^f = \text{atan}\left(\frac{\partial \hat{h}_f^c}{\partial \hat{y}}\right) \tag{4}$$

where the superscript c indicates the centroidal axis of the tow, and the partial derivatives are:

$$\frac{\partial \hat{h}_w^c}{\partial \hat{x}} = -\frac{\pi \hat{b}}{2} \operatorname{sign}(\hat{y}) \cos \pi \hat{x}$$

$$\frac{\partial \hat{h}_f^c}{\partial \hat{y}} = \frac{\pi \hat{b}}{2} \operatorname{sign}(\hat{x}) \cos \pi \hat{y} \tag{5}$$

The functions used to describe the domain of the matrix outside of the tows are [see Figure 5(b)]:

$$\hat{h}_m(n,\hat{x},\hat{y}) = \begin{cases} \min\left(\hat{h}_f(n,\hat{x},\hat{y}),\ \hat{h}_w(n,\hat{x},\hat{y})\right) & n = -1 \\ \max\left(\hat{h}_f(n,\hat{x},\hat{y}),\ \hat{h}_w(n,\hat{x},\hat{y})\right) & n = +1 \end{cases} \tag{6}$$

A 3-D isometric view of the geometry represented via the above surface functions is given in Figure 7. In the figure, cross sections performed at seven locations along the y-axis are shown indicating the potency of the current geometry model in capturing the 2-D undulating woven bundle morphology. The figure of the repeating unit-cell illustrates the complexity of the woven geometry model. Note that the tow cross sections are not symmetric about the tow major axis in general, which is most evident in Sections 3 and 5. Sections 1 and 7 also show that the interbundle matrix is not symmetric about the xy plane.

Note that Figures 4 and 7 as well as Equation (1) do not include a flat bundle region as in most prior models [6–10,12,14,18,19]. Ishikawa and Chou [9] introduced the flat region in the one-dimensional fiber undulation model in order to model twill and satin weaves as well as the plain weave. Plain weave composites that are manufactured by first interlacing "loose" bundles of fibers and then introducing the matrix will tend to maintain the sinusoidal top and bottom profile of the tow cross sections. The above observation appears to be consistent with the plain weave morphologies reported in the literature which do not exhibit the flat bundle region introduced by Ishikawa and Chou. As such, the unit-cell geometry model developed above for plain weave composites does not include the flat bundle region. However, for the less common case of plain weave composites that do possess these flat regions the PW-BDU model may be easily extended to include such a feature. The model may also be extended to include the twill and satin configurations by breaking the geometry into subregions, and applying this model for the undulating subregion.

2.2 Woven Composite Constituent Properties

As discussed earlier in this work, the main objective of this study is to develop a

general and realistic model that can be used to predict with sufficient accuracy the effective elastic response of both *soft*- and *stiff*-matrix woven systems. Due to the CVI technique required to fabricate ceramic matrix woven composites, *stiff*-ceramic matrix systems tend to possess more complex microstructures than that of *soft*-polymer matrix composites. Here we consider woven systems that exhibit rather complicated microstructures similar to that observed by Zok et al. [1], Steyer and Zok [2], and McNulty and Zok [3] and shown in the micrographs in Figure 1 with the intent of developing models which encompass a wide variety of configurations.

The DuPont system shown in Figure 1 was fabricated using a CVI technique. The fabrication process, a detailed description of which can be found elsewhere [2–5], involves several steps including the selection of fiber reinforcements and their weaving into dry fiber bundles, the overlay of matrix free woven bundle mats, the selection and placement of the fiber coating, and the introduction of the matrix material both within and between bundles through CVI techniques and the application of an overall protective coating. As evident by the micrographs

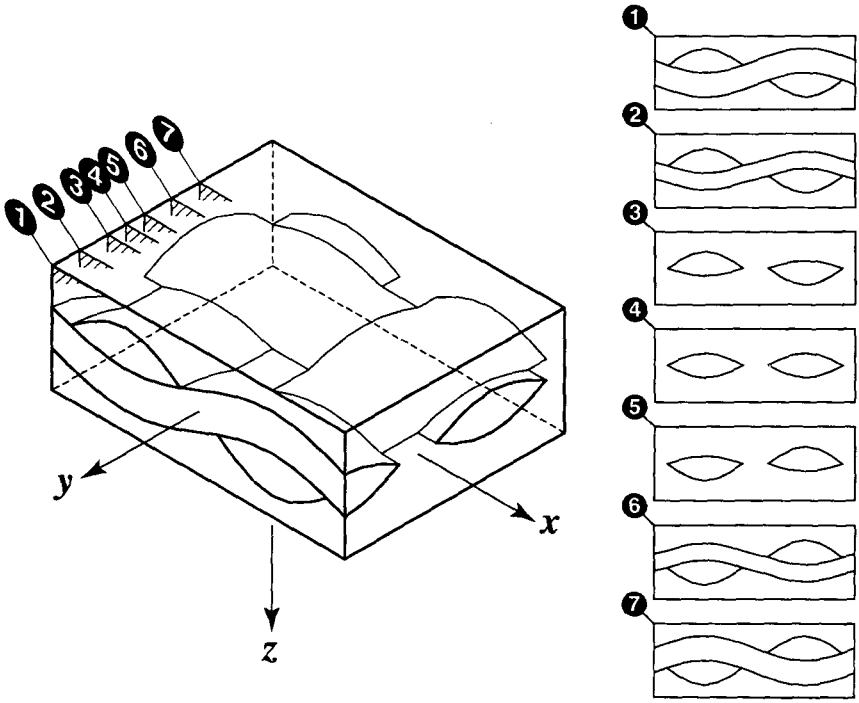

Figure 7. *Three-dimensional isometric view of the woven unit-cell and a sequence of cross-sectional slices.*

shown in Figure 1, the above multi-step fabrication process gives rise to a rather complex microstructure associated with ceramic matrix woven composite laminates. For example, during the introduction of the matrix material, and due to the presence of a rather dense network of fibers, fiber bundles may be only partially infiltrated resulting in a disperse population of bundle porosity whose size and density is controlled by the fiber diameter and bundle fiber volume fraction. In addition, much larger processing voids appear to develop in the matrix region between bundles. The size and shape of these matrix voids clearly depend on the bundle size and shape as well as on the overall woven morphology and processing condition.

For generality purposes, in this work we shall model the complex woven microstructure shown in Figure 1 which exhibits the micro-structural features discussed above using the model unit-cell shown in Figure 8. At the mesoscopic level, the model incorporates distinct features such as the fill and warp tows and the porous interbundle matrix which is allowed to contain large matrix voids. At the micro-structural level, the tows are themselves considered to exhibit a rather complex microstructure. As shown in the bundle schematic on the top of the figure, each bundle is comprised of coated fiber reinforcements, a porous bundle matrix and an overall bundle coating. The above features were included as needed to realistically model a class of woven ceramic composites of the type shown in Figure 1.

The woven morphology shown in Figure 8 can be fully described using the surface functions presented earlier in this work. At the same time, the woven cell microconstituents include in a hierarchical order the following elements. The matrix impregnated fiber bundles represent in a macroscopic mechanical sense an orthotropic material entity with directional effective properties obtained through the proper micromechanics of unidirectionally fiber reinforced composites. In this model, the fiber reinforcements can in general be transversely isotropic with E_L^f, ν_L^f, and G_L^f representing the longitudinal fiber elastic modulus, Poisson's ratio, and shear modulus respectively, and E_T^f and ν_T^f denoting the fiber transverse elastic modulus and Poisson's ratio. As seen in Figure 8, this model also accounts for the presence of a uniform elastically isotropic fiber coating layer of modulus E_{fc} and Poisson's ratio ν_{fc}. As a result of the CVI processing technique the bundle matrix material is the same as the matrix material between bundles (interbundle matrix) and is characterized by an isotropic modulus E_m and Poisson's ratio ν_m. In addition, the bundle microstructure is shown to exhibit a bundle coating layer with distinct isotropic elastic modulus E_{bc} and Poisson's ratio ν_{bc}. The relative volume occupied by each of the above constituents is described via their respective volume fractions. More specifically, in this study, $C_f = V_f/V_{bundle}$ is defined to be the bundle fiber volume fraction, $C_{fc} = V_{fc}/V_{bundle}$ is used to denote the volume occupied by the fiber coating relative to the total volume occupied by the bundle, $C_{bm} = V_{bm}/V_{bundle}$ represents the bundle matrix vol-

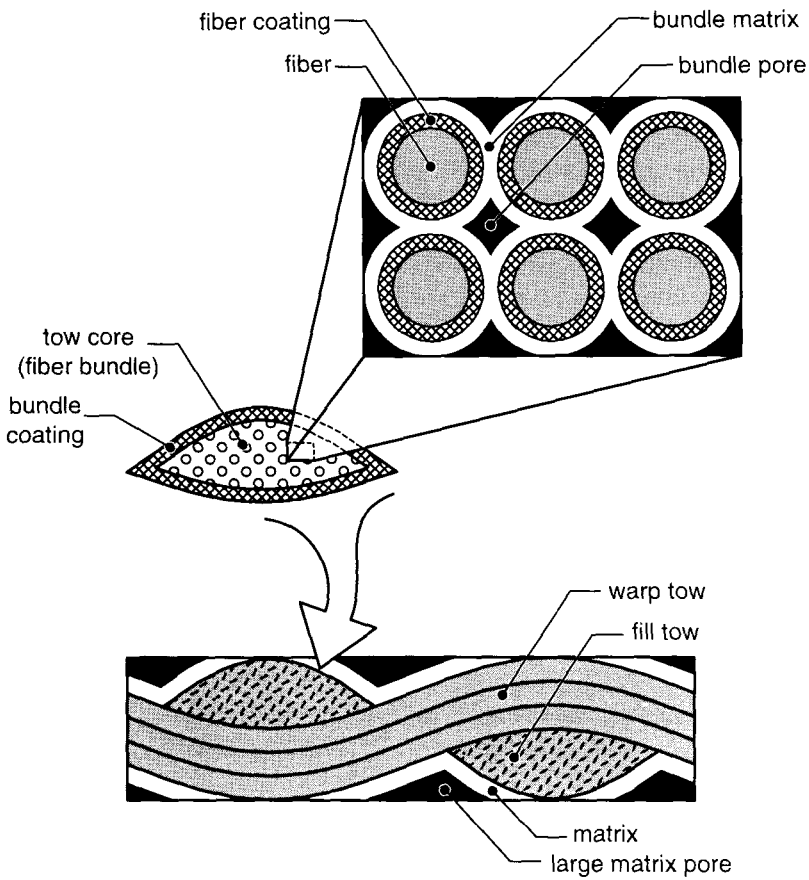

Figure 8. *The cross section model of a single plain weave fabric layer.*

ume fraction, $C_{bc} = V_{bc}/V_{bundle}$ is the volume fraction of the bundle coating layer, and $C_{bp} = V_{bp}/V_{bundle}$ represents the void or porosity volume fraction within the bundle itself. In addition, the model incorporates as an independent variable, the interbundle matrix volume fraction defined as $C_m = V_{matrix}/(V_{total} - V_{bundles})$, where $V_{total} = ha^2$ is the total volume occupied by the woven unit-cell, and the volume fraction for the interbundle matrix voids or porosity which is defined as $C_{mp} = V_{voids}/(V_{total} - V_{bundles})$. Note that $C_f + C_{fc} + C_{bm} + C_{bp} + C_{bc} = 1$ and $C_m + C_{mp} = 1$. The above independent volume fraction variables are obtained in terms of the unit-cell geometry constants a, b, g, h, and l shown in Figure 4(a).

With the advent of computer image processing technologies, the volume fractions of the bundle microconstituents may be determined with respect to the bun-

dle volume as defined above. In the case of CVI ceramic matrix composites with numerous microphases, it may be the only convenient method to determine the volume fractions of each of the bundle constituents. However, the fiber volume fraction is most often reported relative to the total woven unit-cell volume and may vary along the length of the bundle. In such cases we may define the total fiber volume fraction $\overline{C}_f = V_f / V_{total}$ and compute the bundle fiber volume fraction as $C_f = \overline{C}_f V_{total} / V_{bundles}$. The volume occupied by the bundles must be computed with the aid of the geometry surface functions given by Equations (1) and (2).

Given the input microparameters described above, the effective properties of two distinct large scale phases will be treated in the next two sections. First, we shall study the effective orthotropic elastic response of the bundle or tow phase (see Figure 9) by employing proper bundle micromechanics. The homogenization of the complex bundle microstructure shown in Figure 9 shall be modeled via proper bundle micromechanics in determining the effective mesoscopic elastic response of the homogenized bundle phase. In this case the Hashin CCA model along with the porosity model employed by Bassani will be used to determine the effective properties of the tow. Next, an interbundle matrix model shall be developed as needed to obtain the effective elastic response of the porous interbundle matrix phase.

2.2.1. BUNDLE MICROMECHANICS

The effective mesoscopic response of the tow is calculated in four steps as shown schematically in Figure 10. The structure of the fiber bundle is hierarchical in nature, and thus a hierarchical approach is used to determine the effective properties of the homogenized bundle in a manner similar to that employed by Qiu and Weng [36]. In the first micro-structural modeling step [Figure 10(b)], the properties of the fiber reinforcements and those of

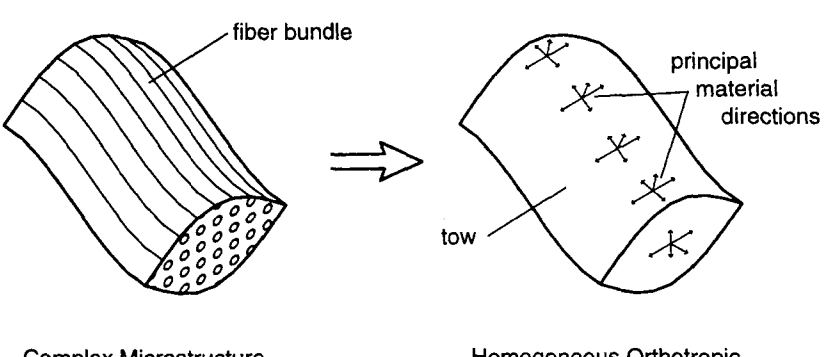

Figure 9. *The complex bundle microstructure homogenization.*

the fiber coating are combined via Hashin's Composite Cylinder Assemblage (CCA) model to obtain the effective properties of the homogenized fiber. During the second step [see Figure 10(c)], the porous solid model employed by Bassani [37] is used to obtain the effective properties of the porous bundle matrix. In the third step [see Figure 10(d)], Hashin's CCA model is used again to obtain the homogenized mesoscopic properties of the fiber bundle. During modeling step #4 [see Figure 10(e)], Hashin's CCA model is employed once more as needed to evaluate the bundle coating effects on the effective elastic response of the homogenized bundle [see Figure 10(e)]. The resulting mesoscopic properties after step #4 are used to obtain the macroscopic effective properties of the woven composite. The details of the above four-step bundle homogenization process shall be presented next.

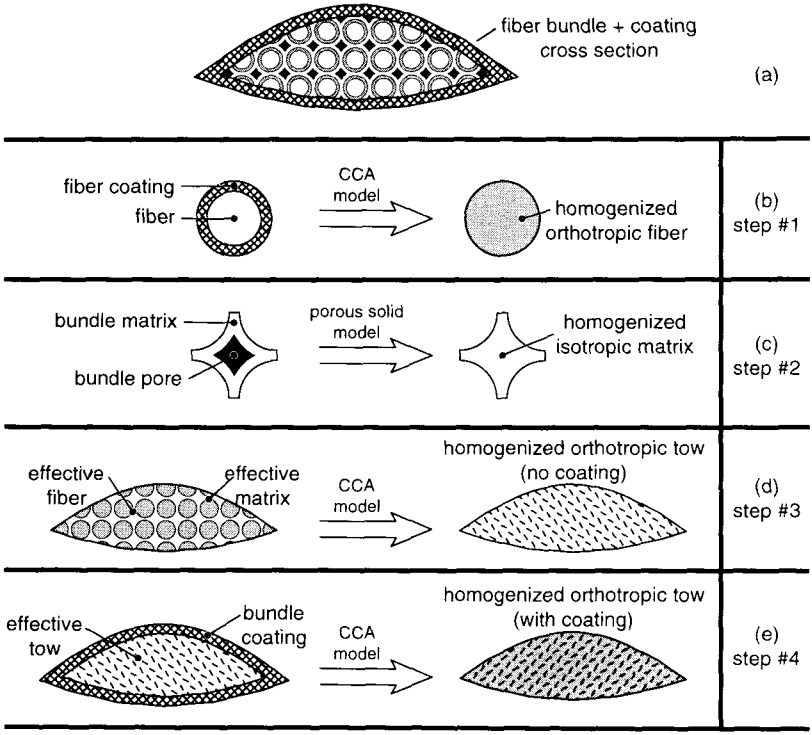

Figure 10. *The hierarchical procedure for determining the effective properties of the tow. (a) The actual fiber bundle with complex microstructure. (b) Step #1—the homogenization of the fiber reinforcement. (c) Step #2—the homogenization of the porous bundle matrix. (d) Step #3—the homogenization of the uncoated bundle. (e) Step #4—the homogenization of the coated bundle.*

As discussed above, in the first step [see Figure 10(b)], the properties of the fiber and fiber coating system are computed using the CCA model of Hashin [38]. The model, which is employed repeatedly in this work, provides for the determination of the effective elastic properties of a transversely isotropic fibrous composite, and is outlined here for completeness.

The CCA model represents the geometry of the fibrous composite as a network of concentric fiber/matrix cylinders. Each composite cylinder is comprised of a solid core corresponding to a fiber surrounded by a matrix coating with constant thickness. Composite cylinders of varying diameters are assembled to fill the volume of the fibrous composite. In general, the CCA model allows for both the fiber and the matrix to be transversely isotropic with the longitudinal matrix axis parallel to the central axis of the composite cylinders. Thus, for this general case we shall assume that the properties of the fiber are taken to be E_1^f, E_2^f, ν_{12}^f, G_{12}^f, G_{23}^f, and k_{23}^f whereas the properties of the matrix, which is also allowed to be orthotropic, are represented by E_1^m, E_2^m, ν_{12}^m, G_{12}^m, G_{23}^m, and k_{23}^m. Here k denotes the plane strain bulk modulus which, for the isotropic case is given by $k = G/(1-2\nu)$, whereas for the transversely orthotropic case is obtained with the aid of the following equations:

$$G_{23} = \frac{E_2}{2(1+\nu_{23})} \quad \text{and} \quad \frac{4}{E_2} = \frac{1}{G_{23}} + \frac{1}{k_{23}} + \frac{4\nu_{12}^2}{E_1} \tag{7}$$

The CCA model yields closed form expressions for the E_1, ν_{12}, G_{12}, and k_{23} directional elastic properties while the fifth property G_{23}, required to fully define the transversely isotropic solid, is bracketed by bounds. All other properties are computed from the above five properties and, if a function of G_{23}, are also bounded, consistent with G_{23}. As will be seen below, the analytical expression obtained using the CCA model involves the fiber and matrix volume fractions which for this general case shall be represented by c_f and c_m respectively. Here the lower case c is used to distinguish the notation used in this general composite cylinder case from the specific model notation of upper case C. For this general case, the first four effective properties of the composite cylinder assemblage are given by:

$$k_{23} = k_{23}^m + \frac{c_f}{\dfrac{1}{k_{23}^f - k_{23}^m} + \dfrac{c_m}{k_{23}^m + G_{23}^m}}$$

$$E_1 = E_1^m c_m + E_1^f c_f + \frac{4(\nu_{12}^f - \nu_{12}^m)^2 c_m c_f}{\dfrac{c_m}{k_{23}^f} + \dfrac{c_f}{k_{23}^m} + \dfrac{1}{G_{23}^m}}$$

$$\nu_{12} = \nu_{12}^m c_m + \nu_{12}^f c_f + \frac{(\nu_{12}^f - \nu_{12}^m)\left(\frac{1}{k_{23}^m} - \frac{1}{k_{23}^f}\right)c_m c_f}{\frac{c_m}{k_{23}^f} + \frac{c_f}{k_{23}^m} + \frac{1}{G_{23}^m}} \tag{8}$$

$$G_{12} = G_{12}^m + \frac{c_f}{\frac{1}{G_{12}^f - G_{12}^m} + \frac{c_m}{2G_{12}^m}}$$

where the subscript 1 represents the longitudinal direction and 2 and 3 are the transverse directions.

The fifth property, i.e., G_{23}, is given in terms of an upper and a lower bound, and thus requires the definition of the following two auxiliary constants G_{23}^a and G_{23}^b, which will be used to define the upper and lower bound estimates as follows:

$$G_{23}^a = G_{23}^m + \frac{c_f}{\frac{1}{G_{23}^f - G_{23}^m} + \frac{c_m(k_{23}^m + 2G_{23}^m)}{2G_{23}^m(k_{23}^m + G_{23}^m)}} \tag{9}$$

$$G_{23}^b = G_{23}^m \left[1 + \frac{c_f(1+\beta_m)}{\rho - c_f\left(1 + \frac{3\beta_m^2 c_m^2}{\alpha c_f^3 + \Delta}\right)}\right] \tag{10}$$

where

$$\beta_m = \frac{k_{23}^m}{k_{23}^m + 2G_{23}^m} \quad \beta_f = \frac{k_{23}^f}{k_{23}^f + 2G_{23}^f} \quad \gamma = \frac{G_{23}^f}{G_{23}^m}$$

$$\alpha = \frac{\beta_\mu - \gamma\beta_f}{1 + \gamma\beta_f} \quad \rho = \frac{\gamma + \beta_m}{\gamma - 1} \quad \Delta = \begin{cases} 1 & G_{23}^f > g_{23}^m \\ -\beta_m & G_{23}^f \le g_{23}^m \end{cases} \tag{11}$$

The bounds on the shear modulus G_{23}, are then computed as:

$$G_{23}^{f} > G_{23}^{m};\quad k_{23}^{f} > k_{23}^{m} \Rightarrow \begin{cases} G_{23}^{-} = G_{23}^{a} \\ G_{23}^{+} = G_{23}^{b} \end{cases}$$

$$G_{23}^{f} < G_{23}^{m};\quad k_{23}^{f} < k_{23}^{m} \Rightarrow \begin{cases} G_{23}^{-} = G_{23}^{b} \\ G_{23}^{+} = G_{23}^{a} \end{cases} \tag{12}$$

where the superscripts – and + indicate lower and upper bounds, respectively. The bounds on two other important properties are then found to be

$$E_2(\pm) = \frac{4k_{23}G_{23}(\pm)}{k_{23} + mG_{23}(\pm)}$$

$$m = 1 + \frac{4k_{23}\nu_{12}^2}{E_1} \tag{13}$$

$$\nu_{23}(\pm) = \frac{k_{23} - mG_{23}(\mp)}{k_{23} + mG_{23}(\mp)}$$

In order to compute the effective properties of the fiber/coating system shown in Figure 10(b), the CCA model of Hashin is applied as an approximation to the single composite cylinder consisting of the fiber and fiber coating. Here the properties of the fiber E_L^f, E_T^f, ν_L^f, ν_T^f, and G_L^f, are substituted for the fiber properties in the CCA model, E_1^f, E_2^f, ν_{12}^f, ν_{23}^f, and G_{13}^f, respectively. At the same time, the isotropic properties of the fiber coating are substituted for the matrix properties in the CCA model, such that $E_1^m = E_2^m = E_{fc}$, $\nu_{12}^m = \nu_{fc}$, and $G_{23}^m = G_{13}^m = G_{fc}$, where $G_{fc} = 1/2E_{fc}/(1+\nu_{fc})$ is the isotropic shear modulus of the fiber coating. Finally, the volume fractions of the fiber c_f, and the matrix c_m, can be expressed in terms of the model constituent volume fractions, such that $c_f = C_f/(C_f + C_{fc})$ and $c_m = C_{fc}/(C_f + C_{fc})$ respectively. The above first step of microconstituent homogenization accounts for the fiber coating effects through the effective properties of the homogeneous orthotropic fiber shown in Figure 10(b).

In the second step of this hierarchical homogenization process [see Figure 10(c)], the effective properties of the porous matrix inside the bundles are computed using the porosity micromechanics model employed by Bassani [37]. As will be discussed later in this study, the porosity model employed by Bassani will also be used to account for the interbundle matrix porosity and is thus presented below for completeness. Bassani [37] employed a model for the effective properties of a porous solid based on the differential self-consistent approximation. The work cited was a study of the linear viscous response of a porous medium which by

analogy to linear elastic porous systems can be used to extract the effective elastic modulus $\bar{E}$, shear modulus $\bar{G}$, bulk modulus $\bar{K}$, and Poisson's ratio $\bar{\nu}$ as a function of the porosity density f. In accordance with Bassani, the above mentioned effective properties are given by

$$\bar{\rho} = 1 - f = \left(\frac{1-\nu}{1-\bar{\nu}}\right)^{1/6}\left(\frac{1+\nu}{1+\bar{\nu}}\right)^{2/3}\left(\frac{1-5\bar{\nu}}{1-5\nu}\right)^{5/6}$$

$$\frac{\bar{G}}{G} = \left[\left(\frac{1+\nu}{1+\bar{\nu}}\right)\left(\frac{1-5\bar{\nu}}{1-5\nu}\right)\right]^{5/3} \tag{14}$$

$$\frac{\bar{E}}{E} = \frac{\bar{G}}{G}\left(\frac{1+\bar{\nu}}{1+\nu}\right)$$

$$\frac{\bar{K}}{K} = \frac{\bar{E}}{E}\left(\frac{1-2\nu}{1-2\bar{\nu}}\right)$$

where f is the porosity and ρ is the material density, with the over-bar ($\bar{}$) denoting the effective properties of the porous elastic medium. As shown in the above equation, all properties are normalized with the respective properties of the fully dense medium, G, E, ν, and K.

In the present case the porosity f is set equal to the volume fraction of microvoids relative to the microvoid/bundle matrix volume, i.e., $f = C_{mp}/(C_{mp} + C_{bm})$. In addition the shear modulus of the homogenized isotropic elastic matrix is given by

$$G_{bm} + \frac{E_{bm}}{2(1+\nu_{bm})} \tag{15}$$

where the subscript bm is used to denote the bundle matrix properties. Thus, for a given porosity f, the porous bundle matrix effective property $\bar{\nu}_{bm} = \bar{\nu}$ is computed numerically from the first non-linear equation of Equations (14) by the Newton-Raphson method. The resulting Poisson's ratio is substituted into the second and third equations to yield the effective properties $\bar{G}_{bm} = \bar{G}$ and $\bar{E}_{bm} = \bar{E}$. For consistency, it is worth mentioning that the bulk moduli K and $\bar{K}$ are not required in the present analysis.

In the third step of this four-step homogenization process [see Figure 10(d)], the effective bundle fiber and effective bundle matrix properties are combined using the CCA model in a manner similar to the first step discussed above as required to

obtain the effective bundle properties. During modeling step #4 [see Figure 10(c)], the bundle coating is introduced using the CCA model by substituting the effective bundle properties determined in step #3 as the fiber properties and by considering the bundle coating as the matrix phase in the CCA model.

For the systems under consideration the upper and lower bounds resulting from the Hashin model appear to be relatively close. In this two-part series of papers, we make use of the lower bounds in the Hashin's models. Thus, the final effective tow properties represent a lower bound resulting from a sequence of lower bound calculations. Clearly, in the above step-by-step micro-structural modeling approach, the CCA model is used three times in obtaining the effective mesoscopic properties of the bundles. The authors are aware of the assumptions and limitations of the CCA model as it relates to an assemblage of concentric composite cylinders of different outer diameters but of identical volume fractions. These conditions are best met during modeling step #3, however, being a higher order model, the CCA model can be used to obtain the directional effective properties of single bimaterial systems such as those involved in modeling steps #1 and #3. It is in light of the above arguments that the CCA model is used during the above steps instead of using first order estimates obtained by employing a simple rule of mixtures approach.

The four-step procedure shown in Figure 10 and discussed above, yields the effective orthotropic elastic properties of the homogenized tow ($E_{11}, G_{22}^{\pm}, G_{12}, G_{23}^{\pm}$, ν_{12}, and $\nu_{23}^{\pm}$), that are used as input to the modified lamination theory for determining the macroscopic in-plane properties of the woven unit-cell (E_x, E_y, G_{xy}, and ν_{xy}). As before, the + and – superscripts are used to denote the upper and lower bound property estimates, as discussed earlier in this section. It is also noted that the numerical subscripts are used to denote the effective tow/bundle properties with respect to its local principal material axes. Likewise, the x and y subscripts correspond with the global woven unit-cell axes, and thus, they denote the effective unit-cell properties.

2.2.2 INTERBUNDLE MATRIX MODEL

The second mesoscopic phase of the woven composite is the effective matrix located outside of the fiber bundles referred to as either the interbundle or inter-tow matrix. The system considered is comprised of pure matrix and large voids (see Figures 1 and 8). The matrix and porosity are combined using the porosity model employed by Bassani [37] to yield the effective properties of a homogeneous isotropic matrix as shown in Figure 11. This model is appropriate for small dispersed porosity distributed in the matrix region outside of the fiber bundles. When relatively large matrix voids exist, as may be the case for many CVI composites, it is recognized that modeling the interbundle matrix as a continuum with its effective properties obtained using the porosity model employed by Bassani may be a crude approximation. Such modeling is more applicable in the case of polymer matrix

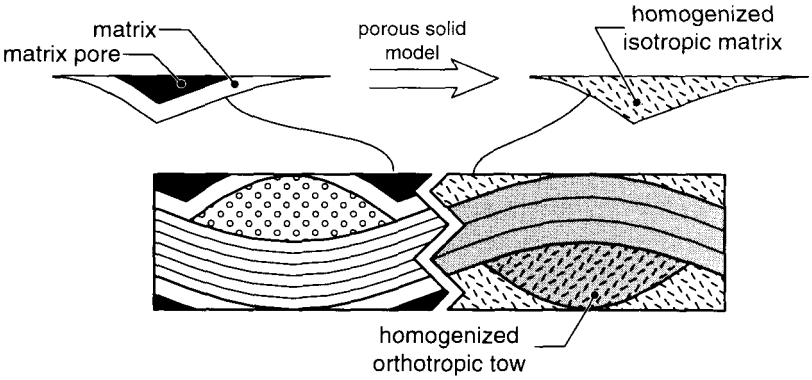

Figure 11. *In this model the porous interbundle matrix is converted to an effective homogeneous and isotropic material using the Bassani porosity model.*

composites where the porosity is comprised of small pores distributed throughout the matrix phase. Clearly, in the case of CVI systems the proposed homogenization scheme provides approximate estimates of the effective interbundle matrix properties. However, more accurate micromechanics models which account for the presence of a network of large discrete voids in the matrix phase between bundles are presented elsewhere [39].

Thus, for this study, the interbundle matrix is considered as an effectively homogeneous isotropic medium whose properties are computed from the Bassani porosity model where the porosity f is replaced by the void volume fraction, C_{mp}. The resulting properties of the effective matrix ($E_{\overline{m}}$ and $\nu_{\overline{m}}$) are then substituted into the model for the macroscopic properties of the effective woven unit-cell (E_x, E_y, G_{xy}, and ν_{xy}) presented in later sections. Here we also note that the subscript $\overline{m}$ implies that the respective properties are those of the homogeneous isotropic effective interbundle matrix, and the x and y subscripts represent the same global directions as described in previous sections.

2.3 Effective Elastic Properties of Woven Composites

In this section, we shall employ a unit-cell approach to determine through analytical means the effective elastic response of CMC woven composites with complex microstructures similar to that shown in Figures 1 and 8, which are also encompassing of typical microstructures associated with PMC woven systems. The unit-cell woven morphology as well as the microconstituent material description presented in the previous sections of this work, will be used in this section in conjunction with a modified lamination theory approach as needed to establish the macroscopic mechanical response due to in-plane uniaxial tension and shear loads

of the heterogeneous woven unit-cell shown in Figures 8 and 12. The load-deformation relations for the heterogeneous woven cell will be compared to the response under the same loading of a homogeneous orthotropic continuum which occupies the same volume in the undeformed state as that occupied by the reference heterogeneous woven unit-cell. Through this standard material properties averaging process, we shall establish the relationship between the effective elastic properties E_x, E_y, ν_{xy}, ν_{yx}, G_{xy} associated with the homogeneous orthotropic plate shown in Figure 12, and the unit-cell microstructure including the unit-cell geometry and microconstituent effects. Consistent with other studies [12–14,19], a modified lamination theory, which utilizes the classical lamination mechanics applied over a laminate column extracted from the reference volume occupied by the woven unit-cell, will be used to assess the mechanical elastic response of the micro-structurally complex unit-cell. As such, the implementation of this modified lamination theory shall be presented next.

2.4 Modified Lamination Theory Applied to 2-D Woven Composites

The modified lamination theory involves the assumption that the classical lamination theory holds for the woven system shown in Figure 13. Initially, the woven unit-cell shown in Figure 13(a) is assumed to have a small aspect ratio of h/l. Next, we consider a differential column element extracted from the woven unit-cell [see Figure 13(a)] of length dx, width dy, and height h as shown in Figure 13(b). This column element exhibits a layer structure which varies with position x and y consistent with the unit-cell woven microstructure. As the differential lengths dx and dy go to zero the layers in the column are assumed to approach constant thickness t_i. In the development of this model, the mechanical elastic response of the layered

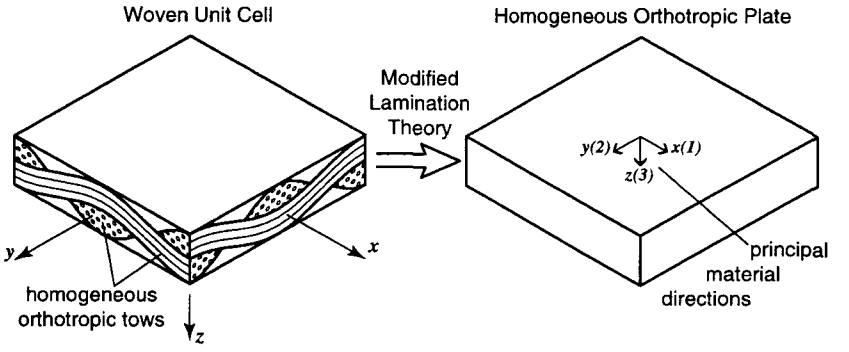

Figure 12. *The macroscopic effective properties of the woven unit-cell are computed as a function of the effective mesoscopic elastic properties of the tow and interbundle matrix phases.*

column element shown in Figure 13(b) will be evaluated using the classical lamination theory. The resultant forces and moments as well as the mid-plane strains and curvatures are allowed to be different for each column and are thus treated as functions of x and y. The overall response of the woven unit-cell will then be obtained through a two-directional integration of the elastic response of the layered

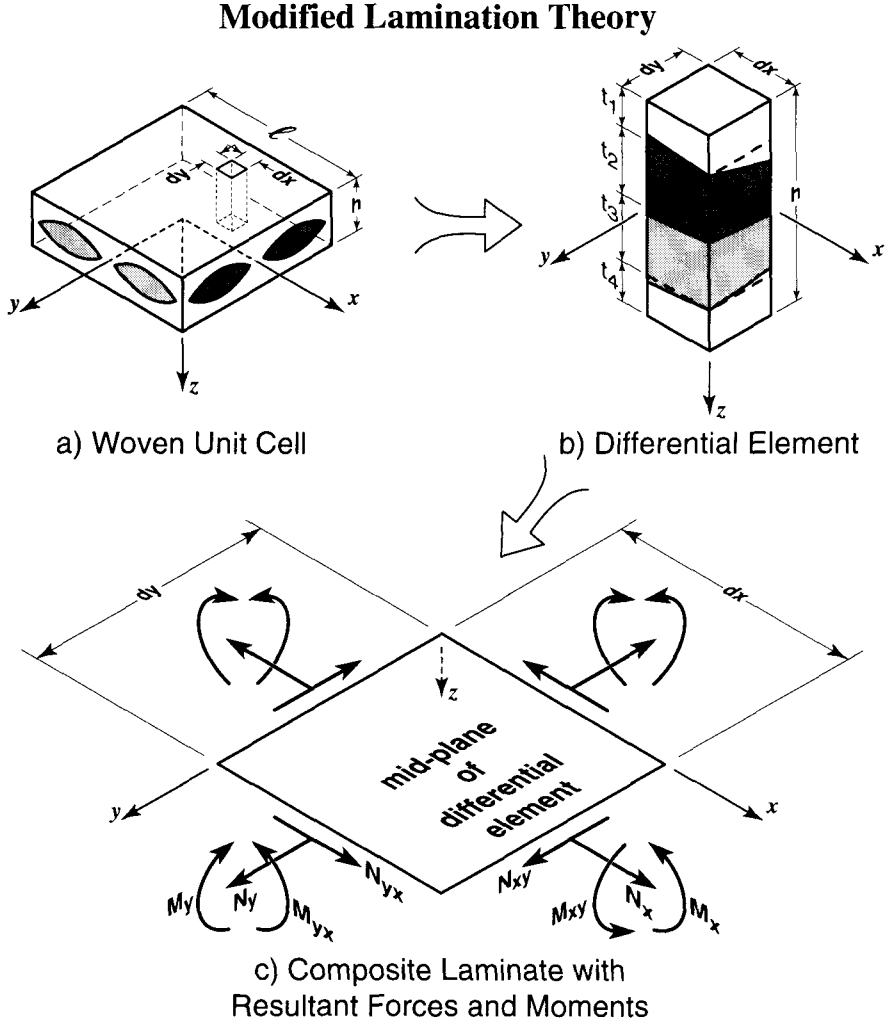

Figure 13. *The modified lamination theory. (a) The woven unit-cell. (b) A differential "column" extracted from the woven unit-cell. (c) The differential column mid-plane used to model the structure as a composite laminate.*

column. This approach allows for the spatial variations of the microconstituents by considering the proper layered column for each (x,y) coordinate pair within the woven unit-cell. In addition, the above approach can also be used to asses the effects of large discrete matrix voids as well as the effects of the presence of bundle/matrix delamination on the overall mechanical response of the woven unit-cell. These latter modeling aspects are addressed elsewhere [39].

As mentioned in Reference [39], in this study it is assumed that the layers comprising each column element within the unit-cell domain, are of constant thickness over the differential lengths dx and dy. The elemental column layer thicknesses are evaluated using the unit-cell geometry functions which yield the bundle/matrix top and bottom interfaces as a function of position (x,y). The elastic properties of the bundle elemental layers are taken to be the orthotropic directional bundle properties obtained through the bundle micromechanics whereas the properties of the porous matrix material between bundles are taken to be the isotropic effective properties of the porous matrix continuum. As discussed in the bundle micromechanics section of this work, the effects of bundle matrix porosity, C_{bp}, bundle fiber coating as measured through the associated volume fraction C_{fc}, and bundle coating measured through C_{bc} are accounted for, through the bundle directional effective properties assigned to the bundle elemental layers. In light of the above assumptions and material considerations, we now proceed to present the development of the unit-cell mechanics using the modified lamination theory approach.

Based on the classical lamination theory, the strains of the elemental layered column are obtained in terms of the mid-plane elemental strains $\{\varepsilon^0(x,y)\}^T = \{\varepsilon_x^0(x,y), \varepsilon_y^0(x,y), \gamma_{xy}^0(x,y)\}$ and curvatures $\{\kappa^0(x,y)\}^T = \{\kappa_x^0(x,y), \kappa_y^0(x,y), \kappa_{xy}^0(x,y)\}$ such that

$$\begin{Bmatrix} \varepsilon_x(x,y,z) \\ \varepsilon_y(x,y,z) \\ \gamma_{xy}(x,y,z) \end{Bmatrix} = \begin{Bmatrix} \varepsilon_x^0(x,y) \\ \varepsilon_y^0(x,y) \\ \gamma_{xy}^0(x,y) \end{Bmatrix} + z \begin{Bmatrix} \kappa_x^0(x,y) \\ \kappa_y^0(x,y) \\ \kappa_{xy}^0(x,y) \end{Bmatrix} \tag{16}$$

where

$$\varepsilon_x^0(x,y) = \frac{\partial u_0(x,y)}{\partial x}$$

$$\varepsilon_y^0(x,y) = \frac{\partial v_0(x,y)}{\partial y} \tag{17}$$

$$\gamma^{0}_{xy}(x,y) = \frac{\partial u_0(x,y)}{\partial y} + \frac{\partial v_0(x,y)}{\partial x}$$

and

$$\kappa^{0}_{x}(x,y) = -\frac{\partial^2 w_0(x,y)}{\partial x^2}$$

$$\kappa^{0}_{y}(x,y) = -\frac{\partial^2 w_0(x,y)}{\partial y^2} \tag{18}$$

$$\kappa^{0}_{xy}(x,y) = -2\frac{\partial^2 w_0(x,y)}{\partial x \partial y}$$

In the above expressions, $u_0(x,y)$, $v_0(x,y)$, and $w_0(x,y)$ represent the x, y, and z displacement components associated with the mid-plane of the differential element shown in Figure 13. The stress-strain relation for material points within layer k is given by

$$\begin{Bmatrix} \sigma_x \\ \sigma_y \\ \tau_{xy} \end{Bmatrix}_k = \begin{bmatrix} \overline{Q}_{11} & \overline{Q}_{12} & 0 \\ \overline{Q}_{21} & \overline{Q}_{22} & 0 \\ 0 & 0 & \overline{Q}_{66} \end{bmatrix}_k \begin{Bmatrix} \varepsilon_x \\ \varepsilon_y \\ \gamma_{xy} \end{Bmatrix} \tag{19}$$

or

$$\begin{Bmatrix} \sigma_x \\ \sigma_y \\ \tau_{xy} \end{Bmatrix}_k = \begin{bmatrix} \overline{Q}_{11} & \overline{Q}_{12} & 0 \\ \overline{Q}_{21} & \overline{Q}_{22} & 0 \\ 0 & 0 & \overline{Q}_{66} \end{bmatrix}_k \begin{Bmatrix} \varepsilon^{0}_{x} \\ \varepsilon^{0}_{y} \\ \gamma^{0}_{xy} \end{Bmatrix} + z \begin{bmatrix} \overline{Q}_{11} & \overline{Q}_{12} & 0 \\ \overline{Q}_{21} & \overline{Q}_{22} & 0 \\ 0 & 0 & \overline{Q}_{66} \end{bmatrix}_k \begin{Bmatrix} \kappa^{0}_{x} \\ \kappa^{0}_{y} \\ \kappa^{0}_{xy} \end{Bmatrix} \tag{20}$$

The local plane-stress stiffness matrix $[\overline{Q}]$ can be derived using a compliance approach with the aid of Reference [40], and are presented in References [7,10,12] as

$$[\overline{Q}] = \begin{bmatrix} \dfrac{E_x}{D} & \dfrac{\nu_{xy}E_y}{D} & 0 \\ \dfrac{\nu_{xy}E_y}{D} & \dfrac{E_y}{D} & 0 \\ 0 & 0 & G_{xy} \end{bmatrix} \tag{21}$$

where $D = 1 - \nu_{xy}\nu_{yx}$, and the plane-stress moduli can be expressed in terms of the direction cosines $l_y = \cos(\theta_y)$ and $m_y = \sin(\theta_y)$ and the principal properties E_1, E_2, E_3, G_{23}, G_{13}, G_{12}, ν_{21}, ν_{23}, and ν_{13} as follows:

$$\begin{aligned} E_x &= \left[\frac{l_y^4}{E_1} + l_y^2 m_y^2\left(\frac{1}{G_{13}} - \frac{2\nu_{13}}{E_1}\right) + \frac{m_y^4}{E_4}\right]^{-1} \\ E_y &= E_2 \\ \nu_{yx} &= l_y^2\nu_{21} + m_y^2\nu_{23} \\ G_{xy} &= \left(\frac{l_y^2}{G_{12}} + \frac{m_y^2}{G_{23}}\right)^{-1} \end{aligned} \tag{22}$$

Although not mentioned in References [7,10,12], the above equations are valid under plane-stress conditions. Alternatively, a stiffness approach may be employed to transform the stiffnesses and is presented in References [9] and [20]. In the above references, however, several non-zero off axis terms were assumed to be zero. As such, a rigorous re-derivation of the transformation equations using a stiffness approach is presented elsewhere [41].

The stress resultants exerted over a length dx and width dy of the elemental column is shown schematically in Figure 13(c) and can be obtained at every point (x,y) in terms of the elemental mid-plane strains $\varepsilon^0(x,y)$, curvatures $\kappa^0(x,y)$, and elemental column laminate stiffnesses $A_{ij}(x,y)$, $B_{ij}(x,y)$, and $D_{ij}(x,y)$, with the indices i and j each varying over the range 1, 2, and 6. Thus, the element column laminate constitutive relation takes the classical form

$$\begin{Bmatrix} N_x \\ N_y \\ N_{xy} \\ M_x \\ M_y \\ M_{xy} \end{Bmatrix}(x,y) = \begin{bmatrix} A_{11} & A_{12} & 0 & B_{11} & B_{12} & 0 \\ A_{21} & A_{22} & 0 & B_{21} & B_{22} & 0 \\ 0 & 0 & A_{33} & 0 & 0 & B_{33} \\ B_{11} & B_{12} & 0 & D_{11} & D_{12} & 0 \\ B_{21} & B_{22} & 0 & D_{21} & D_{22} & 0 \\ 0 & 0 & B_{33} & 0 & 0 & D_{33} \end{bmatrix}(x,y) \begin{Bmatrix} \varepsilon_x^0 \\ \varepsilon_y^0 \\ \gamma_{xy}^0 \\ \kappa_x^0 \\ \kappa_y^0 \\ \kappa_{xy}^0 \end{Bmatrix}(x,y) \quad (23)$$

where the notation (x,y) implies that all preceding vector or matrix entries are functions of the spatial coordinates x and y. The spatially varying column laminate stiffnesses are given by:

$$A_{ij}(x,y) = \int_{h^b(x,y)}^{h^t(x,y)} \overline{Q}_{ij}(x,y,z)\,dz$$

$$B_{ij}(x,y) = \int_{h^b(x,y)}^{h^t(x,y)} \overline{Q}_{ij}(x,y,z)\,z\,dz \quad (24)$$

$$D_{ij}(x,y) = \int_{h^b(x,y)}^{h^t(x,y)} \overline{Q}_{ij}(x,y,z)\,z^2\,dz$$

where $\overline{Q}_{ij}$ are the transformed local stiffnesses which may be different for each layer and thus are functions of z. In addition, the $\overline{Q}_{ij}$ terms are associated with a differential column located at position (x,y) and thus are also functions of x and y due to the undulation of the tows. The terms h^t and h^b represent the distances in the z direction from the mid-plane to the top and bottom surfaces respectively of a column positioned at (x,y), while the quantity $h^t - h^b$ represents the overall height of the column. Each of the overall height quantities $h^t(x,y)$, $h^b(x,y)$, and $h^t(x,y) - h^b(x,y)$ may in general be allowed to vary with respect to x and y, but in this study are kept fixed at constant $h/2$, $-h/2$, and h, respectively. Note that the resulting composite stiffnesses A_{ij}, B_{ij}, and D_{ij} are for a differential column positioned at (x,y), and are themselves functions of x and y.

In the case where the local stiffnesses $\overline{Q}_{ij}$ are constant through the thickness of each layer within a column, Equations (24) may be reduced to:

$$A_{ij}(x,y) = \sum_{k=1}^{\eta(x,y)} (\overline{Q}_{ij})_k \{(h^t)_k - (h^b)_k\}$$

$$B_{ij}(x,y) = \frac{1}{2} \sum_{k=1}^{\eta(x,y)} (\overline{Q}_{ij})_k \{(h^t)_k^2 - (h^b)_k^2\} \tag{25}$$

$$D_{ij}(x,y) = \frac{1}{3} \sum_{k=1}^{\eta(x,y)} (\overline{Q}_{ij})_k \{(h^t)_k^3 - (h^b)_k^3\}$$

with $(\overline{Q}_{ij})_k$ representing the local transformed stiffnesses of the kth layer, and $(h^t)_k$ and $(h^b)_k$ representing the distance in the z direction to the top and bottom surfaces, respectively, of the kth layer of the elemental column positioned at the location (x,y). Each of the terms of $(\overline{Q}_{ij})_k$ as well as $(h^t)_k$ and $(h^b)_k$ are in general functions of x and y. Also in the above stiffness definitions, $\eta(x,y)$ indicates that the layered morphology may indeed change with position (x,y) in a way such that the number of layers $\eta(x,y)$ contained within the associated elemental column may also change with the column position. As an extreme example one can think of the column positioned at the center of the unit-cell at $x = y = 0$ may be comprised of only one layer made of interbundle matrix material. On the other extreme, all elemental columns located at the four corners of the unit-cell could be comprised of four layers, the top and bottom of which are made out of interbundle matrix material whereas the two middle layers are comprised of effective bundle material with potentially different directional properties as a result of different out-of-plane bundle orientations.

Here we point out that the surface functions given by Equations (1), (2), and (6) were developed such that the single function $h_f(1,x,y)$ describes the top surface of the fill tow everywhere in the domain of the unit-cell. Likewise, $h_f(-1,x,y)$ is the bottom surface of the fill tow and $h_w(1,x,y)$ and $h_w(-1,x,y)$ are the top and bottom surfaces respectively of the warp tow. In the case of the matrix, $h_m(1,x,y)$ is the interface surface between the tops of the tows and the bottom of the upper region matrix, and $h_m(-1,x,y)$ is the interface between the bottoms of the tows and the top of the lower region matrix. The fill and warp tows are each treated as single layers within a column, while the matrix is treated as two separate layers, an upper and lower layer. The top surface of the upper matrix is fixed at a constant position $h/2$ while the bottom surface of the upper matrix is equal to $h_m(1,x,y)$. The top surface of the lower matrix is equal to $h_m(-1,x,y)$ while the

bottom surface of the lower matrix is fixed at a constant position $-h/2$. A final important feature of the surface functions is that they collapse to zero for every location x and y at which the respective layer does not exist. As a result we allow $h(x,y)$ to be constant and equal to 4 for each elemental column, and substitute the following surface heights:

$$\begin{aligned}
&\text{For layer \#1} \rightarrow \quad (h^b)_1 = -h/2 \qquad (h^t)_1 = h_m(-1,x,y)\\
&\text{For layer \#2} \rightarrow \quad (h^b)_2 = h_f(-1,x,y) \quad (h^t)_2 = h_f(+1,x,y)\\
&\text{For layer \#3} \rightarrow \quad (h^b)_3 = h_w(-1,x,y) \quad (h^t)_3 = h_w(+1,x,y)\\
&\text{For layer \#4} \rightarrow \quad (h^b)_4 = h_m(+1,x,y) \quad (h^t)_4 = +h/2
\end{aligned} \tag{26}$$

where the numerical subscript indicates the layer to which the term applies. For consistency, it is mentioned that the layers within each elemental column are numbered in ascending order starting at the bottom of the unit-cell. In regions that have less than four layers as described above, the non-existent layers are included but have zero thickness. Also note that the order of layers two and three may be reversed depending on the location in the unit-cell, but this is automatically taken care of by the surface functions.

When using the above unit-cell shape function equations, the column stiffnesses associated with the (x,y) position take the simplified non-dimensional form

$$\begin{aligned}
\hat{A}_{ij} &= \left[\hat{h} + \hat{h}_m^- - \hat{h}_m^+\right]\hat{\bar{Q}}_{ij}^{\,m} + \left[\hat{h}_f^+ - \hat{h}_f^-\right]\hat{\bar{Q}}_{ij}^{\,f} + \left[\hat{h}_w^+ - \hat{h}_w^-\right]\hat{\bar{Q}}_{ij}^{\,w}\\
\hat{B}_{ij} &= \frac{1}{2}\left[\left(\hat{h}_m^-\right)^2 - \left(\hat{h}_m^+\right)^2\right]\hat{\bar{Q}}_{ij}^{\,m} + \frac{1}{2}\left[\left(\hat{h}_f^+\right)^2 - \left(\hat{h}_f^-\right)^2\right]\hat{\bar{Q}}_{ij}^{\,f}\\
&\quad + \frac{1}{2}\left[\left(\hat{h}_w^+\right)^2 - \left(\hat{h}_w^-\right)^2\right]\hat{\bar{Q}}_{ij}^{\,w}\\
\hat{D}_{ij} &= \frac{1}{3}\left[2\left(\frac{\hat{h}}{2}\right)^3 + \left(\hat{h}_m^-\right)^3 - \left(\hat{h}_m^+\right)^3\right]\hat{\bar{Q}}_{ij}^{\,m} + \frac{1}{3}\left[\left(\hat{h}_f^+\right)^3 - \left(\hat{h}_f^-\right)^3\right]\hat{\bar{Q}}_{ij}^{\,f}\\
&\quad + \frac{1}{3}\left[\left(\hat{h}_w^+\right)^3 - \left(\hat{h}_w^-\right)^3\right]\hat{\bar{Q}}_{ij}^{\,w}
\end{aligned} \tag{27}$$

where the hat (^) symbol is used to denote normalized quantities consistent with the normalizing convention discussed below. Also in the above stiffness expressions, $\hat{h}$ represents the normalized height of the woven unit-cell, $\hat{h}_f$, $\hat{h}_w$, and $\hat{h}_m$ are the normalized shape functions for the fill bundle, warp bundle, and matrix phases respectively, the superscripts plus or minus are used to denote the top ($n = +1$) and bottom ($n = -1$) surfaces for the respective faces and $\hat{\bar{Q}}^{f}_{ij}$, $\hat{\bar{Q}}^{w}_{ij}$, and $\hat{\bar{Q}}^{m}_{ij}$ are the normalized column layer elastic stiffnesses transformed as discussed in Section 2.4 using the fiber orientation given by Equations (4). Here we note that the above expressions for the composite stiffnesses apply throughout the domain of the unit-cell, and represent a substantial simplification over the expressions presented in References [12–14].

The non-dimensionalization of the above stiffnesses was obtained in accordance with the following convention used in this study. All physical distances are normalized with respect to a reference length a which as shown in Figure 4(a) represents the bundle undulation wave length, i.e.,

$$\hat{x}_i = \frac{x_i}{a} \tag{28}$$

with $i = 1,2,3$ representing the x, y, and z coordinates respectively. In accordance with the above convention the non-dimensional unit-cell is sketched in Figure 4(b) where $\hat{h} = h/a$, $\hat{l} = l/a$, $\hat{a} = a/a = 1$, $\hat{g} = g/a$, and $\hat{b} = b/a$. The elastic stiffnesses are non-dimensionalized with respect to a reference modulus which in this study is taken to be the longitudinal fiber modulus E^{f}_{L}. Thus, the non-dimensional elastic constants take the form:

$$\hat{\bar{Q}}^{k}_{ij} = \frac{\hat{\bar{Q}}^{k}_{ij}}{E^{f}_{L}} \tag{29}$$

where i and j vary from 1, 2 and 6 and k becomes f, w, and m representing the fill, warp and interbundle porous matrix phases. In light of Equations (28) and (29) the non-dimensional laminate stiffnesses for the elemental column positioned at $(\hat{x}, \hat{y})$ are:

$$\begin{Bmatrix} \hat{\varepsilon}^{0}_{x} \\ \hat{\varepsilon}^{0}_{y} \\ \hat{\gamma}^{0}_{xy} \end{Bmatrix} = \begin{Bmatrix} \varepsilon^{0}_{x} \\ \varepsilon^{0}_{y} \\ \gamma^{0}_{xy} \end{Bmatrix} \frac{1}{\varepsilon_c} \quad \text{and} \quad \begin{Bmatrix} \hat{\kappa}^{0}_{x} \\ \hat{\kappa}^{0}_{y} \\ \hat{\kappa}^{0}_{xy} \end{Bmatrix} = \begin{Bmatrix} \kappa^{0}_{x} \\ \kappa^{0}_{y} \\ \kappa^{0}_{xy} \end{Bmatrix} \frac{1}{\kappa_c} \tag{30}$$

where ε_c is a characteristic strain, $\kappa_c = \varepsilon_c/a$ is a characteristic curvature, and a is the

half period of the unit-cell. By making use of the constitutive laminate relations given by Equation (23), one can show that the non-dimensional cross-sectional resultant forces and moments are given by

$$\begin{Bmatrix} \hat{N}_x \\ \hat{N}_y \\ \hat{N}_{xy} \end{Bmatrix} = \begin{Bmatrix} N_x \\ N_y \\ N_{xy} \end{Bmatrix} \frac{1}{E_L^f a \varepsilon_c} \quad \text{and} \quad \begin{Bmatrix} \hat{M}_x \\ \hat{M}_y \\ \hat{M}_{xy} \end{Bmatrix} = \begin{Bmatrix} M_x \\ M_y \\ M_{xy} \end{Bmatrix} \frac{1}{E_L^f a^2 \varepsilon_c} \tag{31}$$

It can also be shown that the characteristic strain ε_c is related to the characteristic stress σ_c and the reference modulus E_L^f via the Hooke's law, i.e.,

$$\varepsilon_c = \frac{\sigma_c}{E_L^f} = \frac{\text{characteristic stress}}{\text{characteristic modulus}} \tag{32}$$

Another useful expression for ε_c is that relating the latter quantity to an applied characteristic displacement U such that

$$\varepsilon_c = \frac{U}{a} = \frac{\text{characteristic displacement}}{\text{characteristic length}} \tag{33}$$

Having determined the constitutive behavior of each differential element, the macroscopic behavior of the woven unit-cell is determined by applying a uniform load in the warp direction, and computing either the average resultant load or mid-plane strains and curvatures. Because the microstresses and microstrains are unknown, an assumption about either the mid-plane strains and curvatures or their work conjugate force and moment resultants are employed to enable the computation of the averages. There are four different approaches to averaging the response of the woven unit-cell which are outlined in Table 1. The details behind each integration scheme and the assumptions made can be found in the respective references which are also listed in Table 1. These averaging schemes yield good estimates for the effective response of the unit-cell, but do not accurately model the micro-response of the system which is critical for the prediction of microstress induced damage within the woven unit-cell.

The following is a summary of the equations for the effective stiffnesses and compliances which result from each of the averaging methods. In this model, the integrals that appear in Equations (34) through (37) are to be evaluated numeri-

Table 1. The four averaging schemes used to assess the effective elastic response of the woven unit-cell.

Method	Average	With Respect To	Assuming
1. Parallel [10,14]	$\left\{\begin{matrix}\hat{N}_i\\ \hat{M}_i\end{matrix}\right\}(\hat{x},\hat{y})$	$\hat{x}$ and $\hat{y}$	$\left\{\begin{matrix}\hat{\varepsilon}_i^0\\ \hat{\kappa}_i\end{matrix}\right\} \equiv$ constant
2. Series [10]	$\left\{\begin{matrix}\hat{\varepsilon}_i^0\\ \hat{\kappa}_i\end{matrix}\right\}(\hat{x},\hat{y})$	$\hat{x}$ and $\hat{y}$	$\left\{\begin{matrix}\hat{N}_i\\ \hat{M}_i\end{matrix}\right\} \equiv$ constant
3. Series-Parallel [12]	$\left\{\begin{matrix}\hat{\varepsilon}_i^0\\ \hat{\kappa}_i\end{matrix}\right\}(\hat{x})$	$\hat{x}$	$\left\{\begin{matrix}\hat{N}_i\\ \hat{M}_i\end{matrix}\right\} \equiv$ Function of $\hat{y}$ only
	$\left\{\begin{matrix}\hat{N}_i\\ \hat{M}_i\end{matrix}\right\}(\hat{y})$	$\hat{y}$	$\left\{\begin{matrix}\hat{\varepsilon}_i^0\\ \hat{\kappa}_i\end{matrix}\right\} \equiv$ Function of $\hat{x}$ only
4. Parallel-Series [12]	$\left\{\begin{matrix}\hat{N}_i\\ \hat{M}_i\end{matrix}\right\}(\hat{x})$	$\hat{x}$	$\left\{\begin{matrix}\hat{\varepsilon}_i^0\\ \hat{\kappa}_i\end{matrix}\right\} \equiv$ Function of $\hat{y}$ only
	$\left\{\begin{matrix}\hat{\varepsilon}_i^0\\ \hat{\kappa}_i\end{matrix}\right\}(\hat{y})$	$\hat{y}$	$\left\{\begin{matrix}\hat{N}_i\\ \hat{M}_i\end{matrix}\right\} \equiv$ Function of $\hat{x}$ only

cally. Thus, the following stiffness integration schemes are incorporated in the current model:

Parallel (P-MLT) averaging scheme:

$$\left[\begin{array}{c|c}\overline{A}_{ij} & \overline{B}_{ij}\\ \hline \overline{B}_{ij} & \overline{D}_{ij}\end{array}\right] = \frac{1}{LW}\int_L\int_W \left[\begin{array}{c|c}A_{ij} & B_{ij}\\ \hline B_{ij} & D_{ij}\end{array}\right](x,y)\,dxdy \tag{34}$$

Series (S-MLT) averaging scheme:

$$\left[\begin{array}{c|c}\overline{a}_{ij} & \overline{b}_{ij}\\ \hline \overline{b}^T_{ij} & \overline{d}_{ij}\end{array}\right] = \frac{1}{LW}\int_L\int_W \left[\begin{array}{c|c}a_{ij} & b_{ij}\\ \hline b^T_{ij} & d_{ij}\end{array}\right](x,y)\,dxdy \tag{35}$$

Series-Parallel (SP-MLT) averaging scheme:

$$\left[\begin{array}{c|c}a'_{ij} & b'_{ij}\\ \hline b'^T_{ij} & d'_{ij}\end{array}\right](y) = \frac{1}{W}\int_W \left[\begin{array}{c|c}a_{ij} & b_{ij}\\ \hline b^T_{ij} & d_{ij}\end{array}\right](x,y)\,dx \tag{36}$$

$$\left[\begin{array}{c|c} \overline{A}_{ij} & \overline{B}_{ij} \\ \hline \overline{B}_{ij} & \overline{D}_{ij} \end{array}\right] = \frac{1}{L}\int_L \left[\begin{array}{c|c} A'_{ij} & B'_{ij} \\ \hline B'_{ij} & D'_{ij} \end{array}\right](y)dy$$

Parallel-Series (PS-MLT) averaging scheme:

$$\left[\begin{array}{c|c} A'_{ij} & B'_{ij} \\ \hline B'_{ij} & D'_{ij} \end{array}\right](y) = \frac{1}{W}\int_W \left[\begin{array}{c|c} A_{ij} & B_{ij} \\ \hline B_{ij} & D_{ij} \end{array}\right](x,y)dx$$

$$\left[\begin{array}{c|c} \overline{a}_{ij} & \overline{b}_{ij} \\ \hline \overline{b}^T_{ij} & \overline{d}_{ij} \end{array}\right] = \frac{1}{L}\int_L \left[\begin{array}{c|c} a'_{ij} & b'_{ij} \\ \hline b'^T_{ij} & d'_{ij} \end{array}\right](y)dy \tag{37}$$

where the prime symbol ($'$), is used to imply that the corresponding term is averaged in one direction, remaining a function of the other direction. Also in the above expressions, the bar symbol ($\bar{}$), implies the corresponding term is constant and averaged in both directions. In addition, in the above equations the compliances and stiffnesses are related as follows:

$$\left[\begin{array}{c|c} a_{ij} & b_{ij} \\ \hline b^T_{ij} & d_{ij} \end{array}\right] = \left[\begin{array}{c|c} A_{ij} & B_{ij} \\ \hline B_{ij} & D_{ij} \end{array}\right]^{-1} \tag{38}$$

and the resulting expressions may be non-dimensionalized consistent with the procedure outlined earlier in this paper.

For the case of the plain weave fabric, the average coupling terms ($\overline{b}_{ij}$) equal zero even though the local ($\hat{b}_{ij}$)terms may be nonzero. As a result the effective in-plane properties of the woven unit-cell can be extracted from the ($\overline{a}_{ij}$)terms as follows [12]:

$$\hat{E}_x = \frac{1}{\overline{a}_{11}\hat{h}}$$

$$\hat{G}_{xy} = \frac{1}{\overline{a}_{66}\hat{h}} \tag{39}$$

$$\nu_{xy} = -\frac{\overline{a}_{12}}{\overline{a}_{11}}$$

where:

$$E_x = E_L^f \hat{E}_x$$
$$G_{xy} = E_L^f \hat{G}_{xy} \tag{40}$$

The above model was used to perform parameter studies and the results are presented in a companion paper under the title extension, Part II—Results. The next section discusses the formulation of a three-dimensional (3-D) finite element model, which will be used to extract independent numerical estimates of the in-plane woven-cell elastic properties. As mentioned above, the finite element results are reported along with the analytical estimates in a companion paper.

3. THREE-DIMENSIONAL FINITE ELEMENT MODEL

In this section, three-dimensional (3-D) elasticity solutions, associated with the woven unit-cell geometry used in the analytical studies subjected to remote tension and shear loading are obtained with the aid of the method of finite elements. These numerical studies are carried out in a non-dimensional environment consistent with the non-dimensional unit-cell shown in Figure 4(b). The geometry parameters used in the numerical finite element studies are:

$$(a)_{fe} = \hat{a} = \frac{a}{a} = 1$$
$$(b)_{fe} = \hat{b} = \frac{b}{a} \text{ with } 0.0 < \hat{b} \leq 0.5$$
$$(h)_{fe} = \hat{h} = \frac{h}{a} \text{ with } 0.0 < \hat{h} \leq 1.0 \tag{41}$$
$$(l)_{fe} = \hat{l} = \frac{l}{a} = 1$$
$$(g)_{fe} = \hat{g} = \frac{g}{a} \text{ with } 0.0 \leq \hat{g} \leq 0.5$$

where the subscript $(\,)_{fe}$ is used to denote finite element parameters. The material elastic properties are assigned to the fill and warp tows and interbundle matrix in a manner consistent with that used in the development of the analytical model. The effective directional elastic stiffnesses of each tow calculated through the bundle micromechanics are normalized with the reference modulus E_L^f. Thus the bundle normalized properties used in the finite element model are assigned to each material point as the ratio of the actual effective directional property value relative to the longitudinal fiber modulus. This approach preserves the generality of the re-

sults obtained through this model, which can be used to study the elastic response of a family of material combinations, by considering the response of only one material pair. Thus, the directional properties used in both the analytical and numerical models are taken to be

$$\lambda_{1f} = \hat{E}_1 = \frac{E_1}{E_L^f} \qquad \lambda_{4f} = \hat{G}_{12} = \frac{G_{12}}{E_L^f}$$

$$\lambda_{2f} = \hat{E}_2 = \frac{E_2}{E_L^f} \qquad \lambda_{5f} = \hat{G}_{13} = \frac{G_{13}}{E_L^f} \tag{42}$$

$$\lambda_{3f} = \hat{E}_3 = \frac{E_3}{E_L^f} \qquad \lambda_{6f} = \hat{G}_{23} = \frac{G_{23}}{E_L^f}$$

The Poisson's ratios for each of the tows were taken to be $\hat{\nu}_{12} = \nu_{12}$, $\hat{\nu}_{13} = \nu_{13}$, and $\hat{\nu}_{23} = \nu_{23}$. While assigning the above properties to the fill and warp tows consistent with their respective principal orientation, the effective interbundle matrix elastic properties obtained through the previously described porous matrix model, were also normalized with the fiber modulus such that, all finite elements within the interbundle space were assigned the following isotropic elastic constants $\lambda_{mf} = \hat{E}_{\bar{m}} = E_{\bar{m}}/E_L^f$ and $\hat{\nu}_{\bar{m}} = \nu_{\bar{m}}$.

3.1 Geometry Discretization

An automated mesh generator with robust woven unit-cell discretization features, was developed and fully integrated into the in-house technology transfer finite element software DENDRO. Unit-cell geometry meshes comprised of 8-noded, and 20-noded isoparametric brick elements were developed and tested by comparing the DENDRO results to similar results obtained using the commercially available ABAQUS [42] package. Several limiting cases such as the case of an elastically homogeneous unit-cell were also considered in identifying optimal woven unit-cell meshes. Through the above considerations, it was established that the 20-noded isoparametric brick elements gave highly accurate elastic solutions and thus, the above type of 3-D finite element was adopted for the numerical finite element studies reported in this work.

A typical woven unit-cell mesh comprised of 1344, 20-noded isoparametric brick elements with 7290 total number of degrees of freedom is shown in Figure 14. The overall unit-cell woven morphology was established using the shape functions given by Equations (1) and (2). In order to avoid collapsing the thin matrix elements at each of the 8 corners a height of $\hat{h} = 2\hat{b} + 0.005$ was used. The orthotropic material properties within the fill and warp tows were assigned consistent

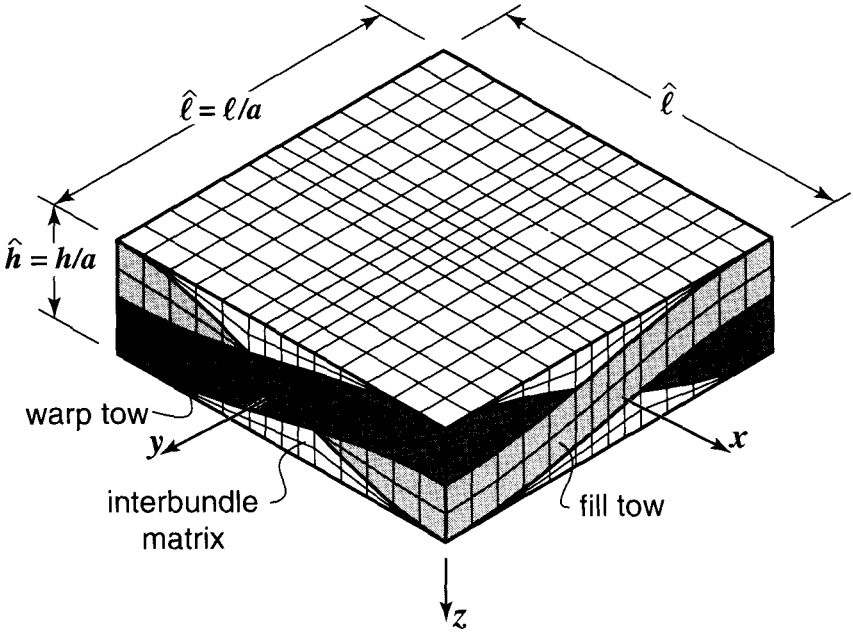

Figure 14. *A typical finite element mesh corresponding to the porous matrix model.*

with the spatially varying directional characteristics of each tow. The principal material directions were obtained using Equations (4) and (5) in combination with additional 0° and 90° rotations about the z-axis. Homogeneous isotropic properties were assigned to the interbundle matrix phase as discussed above. With the aid of the mesh generator, and DENDRO software, element subsets for the fill and warp bundles and interbundle matrix region were developed and used to verify the complex three-dimensional features of the woven-cell microstructure. Internal consistency checks were used to detect and remove coincident nodes along the bundle/matrix interfaces.

Now recall that the analytical model developed earlier in this work can be used to obtain estimates of the in-plane effective elastic properties of the woven unit-cell. These properties include the elastic moduli $\hat{E}_x$, and $\hat{E}_y$, the in-plane shear modulus $\hat{G}_{xy}$ and Poisson's ratio $\hat{\nu}_{xy}$. For comparison purposes, the finite element model developed herein will be used to extract numerical estimates of the same effective properties as those obtained via the analytical scheme. For that purpose we shall now proceed to describe the unit-cell boundary conditions associated with remote pure tension and pure shear loading used in these numerical studies.

3.2 Pure Remote Tension Loading

The finite element elastic solution associated with the unit-cell loaded in the x direction will be used to extract the effective modulus $\hat{E}_x$ and Poisson's ratio $\hat{\nu}_{xy}$. Due to directional symmetry, the above properties can also be used to characterize the elastic response of the unit-cell due to an applied axial tension in the y direction, i.e., $\hat{E}_y = \hat{E}_x$ and $\hat{\nu}_{yx} = \nu_{xy}$. Thus, in this study we shall only consider the case wherein the woven unit-cell is subjected to an overall axial stretching in the x direction. The displacement and traction boundary conditions simulating the above loading case are shown schematically in Figure 15(a), which depicts the top view of the 3-D woven cell. As shown in the above figure, the unit-cell faces at $\hat{y} = \pm\ \hat{l}/2$ and $\hat{x} = -\hat{l}/2$ are restrained as needed to enforce symmetry conditions. More specifically, on the $\hat{x} = -\hat{l}/2$ and $\hat{y} = -\hat{l}/2$ faces, the normal displacement components and their non-work conjugate traction components are taken to be zero. While imposing the above conditions, the $\hat{y} = \hat{l}/2$ unit-cell face is restrained as needed to maintain its planarity during deformation. This condition is enforced by requiring that all finite element nodes located on the above plane deform by the same constant amount, $\hat{u}_y = C$ in the direction normal to the above plane. On the same plane, traction free boundary conditions acting in the x and z directions are also enforced, while the sum of all nodal forces in the y direction is set equal to zero to maintain global equilibrium.

As shown in Figure 15(a), the unit-cell is stretched by an amount equal to the applied characteristic U. When doing such non-dimensional studies, it is often convenient without loss of generality to set the above normalizing characteristic displacement equal to unity. Thus, in this uniaxial tension case, on the unit-cell face at $\hat{x} = \hat{l}/2$ we apply $\hat{u}_x = \hat{U}_x =$ "1" while the transverse

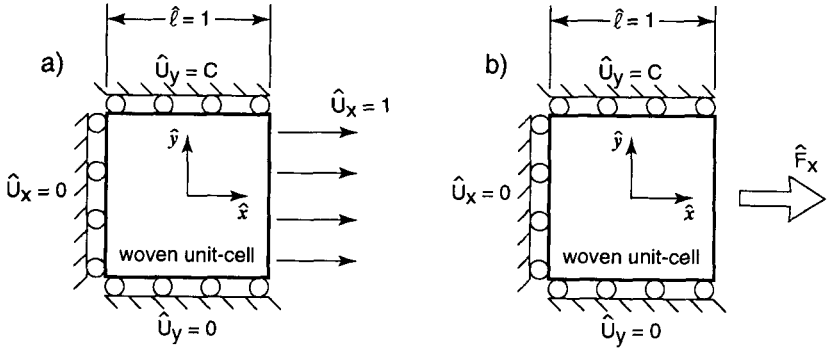

Figure 15. *The displacement boundary conditions corresponding with uniaxial non-dimensional unit extension. (a) The applied unit-displacement. (b) The subsequent reaction force computed from the numerical finite element solution.*

shear nodal forces $\hat{F}_{xy}$ and $\hat{F}_{xz}$, associated with the same unit-cell face, are set to be zero.

In this study, finite element results associated with the response of a single woven ply and results reflecting the response of a multiple-ply laminate comprised of woven plies overlayed with alternating symmetry will be sought (see Figure 2). As such, two different sets of boundary conditions applied on the top ($\hat{z} = +\hat{h}/2$) and bottom ($\hat{z} = +\hat{h}/2$) woven unit-cell surfaces will be used. The single-ply response will be modeled by simply enforcing traction-free conditions on the top and bottom unit-cell surfaces. On the other hand, the multiple-ply laminate response will be modeled by enforcing zero normal displacements on the $\hat{z} = -\hat{h}/2$ unit-cell face while requiring the opposite face to remain planar during deformation.

The effective woven unit-cell elastic properties obtained from the tension case study are given by

$$\hat{E}_x = \frac{\hat{F}_x}{\hat{h}} \quad \text{and} \quad \hat{\nu}_{xy} = -\frac{u_y}{u_x} = -\hat{u}_y \tag{43}$$

where $\hat{F}_x$ is the numerically calculated reaction force resultant acting on the $\hat{x} = \hat{l}/2$ plane as shown in Figure 15(b), $\hat{h}$ is the normalized height of the unit-cell and $\hat{u}_y$ is the computed normalized constant displacement of the unit-cell face at $\hat{y} = \hat{l}/2$. Next, we shall briefly present the shear test model conditions used in extracting the in-plane effective shear modulus $\hat{G}_{xy}$.

3.3 Pure Remote Shear Loading

The pure shear loading model depicted in Figure 16(a) will be used to extract the effective shear modulus for the woven composites under consideration. In this case, the woven unit-cell geometry used in the applied tension studies is subjected to an applied remote shear via the boundary conditions shown in Figure 16(a). In accordance with the above schematic, in-plane geometry antisymmetry conditions are enforced on all vertical faces of the unit-cell. Thus, the $\hat{u}_y$ displacement component for all finite element nodes located on the $\hat{x} = \pm\hat{l}/2$ faces are set to be zero. At the same time, the $\hat{u}_x$ displacement component for all nodes located on the $\hat{y} = -\hat{l}/2$are also set to be zero while all nodes located on the opposite unit-cell face at $\hat{y} = +\hat{l}/2$ are forced to displace by an amount equal to unity, i.e., $\hat{u}_x(\hat{x}, \hat{y} = +\hat{l}/2, \hat{z}) = 1$. As in the case of pure tension, two out-of-plane boundary conditions were considered for the pure shear case simulating the response of a single-ply and the response of symmetrically placed multiple woven plies. In particular, the single-ply studies were performed by considering the top and bottom unit-cell surfaces located at $\hat{z} = \pm\hat{h}/2$ to be traction free thus allowing out-of-plane twisting of the unit-

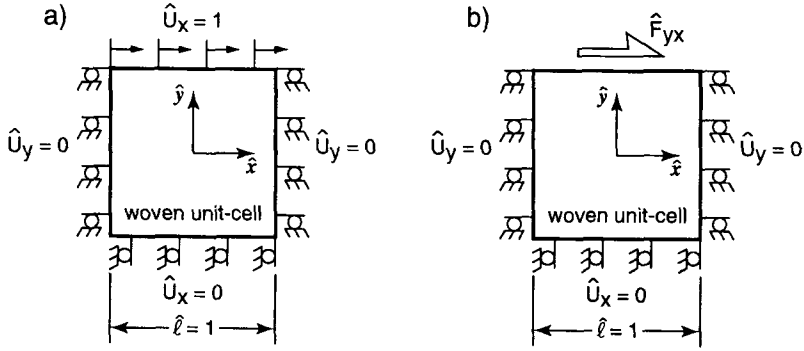

Figure 16. *The displacement boundary conditions corresponding with non-dimensional unit pure shear. (a) The applied unit-displacement. (b) The subsequent reaction force computed from the numerical finite element solution.*

cell. Multiple-ply laminate studies were performed by enforcing zero normal displacements on the bottom unit-cell surface while requiring the top surface to maintain its planarity during deformation.

The effective woven unit-cell elastic shear modulus obtained from the pure shear case study is given by

$$\hat{G}_{xy} = \frac{\hat{F}_{yx}}{\hat{h}} \tag{44}$$

where $\hat{F}_{yx}$ is the numerically calculated reaction force resultant acting on the $\hat{y} = \hat{l}/2$ plane as shown in Figure 16(b) and $\hat{h}$ is the normalized height of the unit-cell.

4. CONCLUSIONS

The framework for the determination of the in-plane effective elastic properties of *soft*- and *stiff*-matrix woven composites has been established analytically via a Modified Lamination Theory (MLT) approach and numerically via a 3-D finite element model. Several micromechanics models were introduced as needed to study the effects of bundle and interbundle matrix porosity, fiber and bundle coatings, as well as the effects of material heterogeneity and woven morphology on the in-plane effective properties. The models developed herein can be used to study the response of both *soft*-polymer and *stiff*-ceramic matrix woven composites exhibiting rather complex microstructures. Effective property results obtained with the aid of these models are reported, compared and discussed in a companion manuscript entitled, Elastic Response of Porous Matrix Plain Weave Fabric Composites: Part II—Results. In addition to establishing the effective elastic response

of woven systems, the current model can also be used to obtain microstress and microstrain unit-cell estimates as needed for the initial evaluation of stress induced damage in CVI ceramic and polymer matrix woven systems.

ACKNOWLEDGEMENTS

Support for this work was provided by the National Science Foundation, Grant No. CMS94-96209. Many discussions with Professor Frank Zok, Professor Rajendra Bordia, and their associates are readily acknowledged. The authors are grateful to Frank Zok for providing the micrographs presented in this work.

REFERENCES

1. Frank Zok, John McNulty, and Todd Steyer. Private communication. Materials Department, University of California, Santa Barbara.
2. T. E. Steyer and F. W. Zok. 1996. "Stress Rupture of A SiC/SiC Composite ." Presented at *The American Ceramic Society 1996 Annual Meeting & Exposition,* Indianapolis, Ind.
3. J. C. McNulty and F. W. Zok. 1996. "Notch Sensitivity of SiC/SiC at Ambient and Elevated Temperatures ." Presented at *The American Ceramic Society 1996 Annual Meeting & Exposition,* Indianapolis, Ind.
4. Rajendra K. Bordia, David H. Roach, and Samuel M. Salamone. 1995. "Crack Growth Resistance of CVI Processed Ceramic Matrix Composites." *Proceedings of ICCM.*
5. Rajendra K. Bordia, David H. Roach, Samuel M. Salamone, and Mark Headinger. "Tensile Properties and Crack Growth Resistance of Ceramic Matrix Composites." *Submitted for publication to the J. Amer. Ceram. Soc.*
6. Takashi Ishikawa and Tsu-Wei Chou. 1982. "Elastic Behavior of Woven Hybrid Composites." *J. Composite Mater.*, 16:2–19.
7. T. Ishikawa and T. W. Chou. 1982. "Stiffness and Strength Behavior of Woven Fabric Composites." *J. Mater. Sci.*, 17:3211–3220.
8. Takashi Ishikawa and Tsu-Wei Chou. 1983. "In-Plane Thermal Expansion and Thermal Bending Coefficients of Fabric Composites." *J. Composite Mater.*, 17:92–104.
9. Takashi Ishikawa and Tsu-Wei Chou. 1983. "One-Dimensional Micromechanical Analysis of Woven Fabric Composites." *AIAA J.*, 21(12):1714–1721.
10. Tsu-Wei Chou and Takashi Ishikawa. 1989. "Analysis and Modeling of Two-Dimensional Fabric Composites." In Tsu-Wei Chou and Frank K. Ko, editors, *Textile Structural Composites: Composite Materials Series,* Volume 3, pp. 209–264. Elsevier Science Publishers B.V.
11. Takashi Ishikawa, Masamichi Matsushima, Youichi Hayashi, and Tsu-Wei Chou. 1985. "Experimental Confirmation of the Theory of Elastic Moduli of Fabric Composites." *J. Composite Mater.*, 19:443–458.
12. N. K. Naik and P. S. Shembekar. 1992. "Elastic Behavior of Woven Fabric Composites: I—Lamina Analysis." *J. Composite Mater.*, 26(15):2196–2225.
13. N. K. Naik and V. K. Ganesh. 1992. "Prediction of On-axes Elastic Properties of Plain Weave Fabric Composites." *Composites Sci. & Tech.*, 45:135–152.
14. Ivatury S. Raju and John T. Wang. 1994. "Classical Laminate Theory Models for Woven Fabric Composites." *J. Composite Tech. & Res.*, 16(4):289–303.
15. S. Shkoller and G. Hegemier. 1995. "Homogenization of Plain Weave Composites Using Two-Scale Convergence." *I. J. Sol. & Struc.*, 32(6-7):783–794.

16. A. Dasgupta and S. M. Bhandarkar. 1994. "Effective Thermomechanical Behavior of Plain-Weave Fabric Reinforced Composites Using Homogenization Theory." *J. Engr. Mater. & Tech.*, 116:99–105.
17. Y. C. Zhang and J. Harding. 1990. "A Numerical Micromechanics Analysis of the Mechanical Properties of a Plain Weave Composite." *Computers and Structures*, 36(5):839–844.
18. John D. Whitcomb. 1991. "Three-Dimensional Stress Analysis of Plain Weave Composites." In T. K. O'Brien, editor, *Composite Materials: Fatigue and Fracture (Third Volume), ASTM STP 1110*, pp. 417–438. American Society for Testing and Materials, Philadelphia.
19. K. Ranji Vaidyanathan, Ajit D. Kelkar, and Jagannathan Sankar. 1993. "Prediction of Elastic Properties of Ceramic Matrix Composites Using a Plain Weave Classical Laminate Theory." *Ceram. Engr. Sci. Proc.*, 14(9-10):1066–1076.
20. Wen-Shyong Kuo and Tsu-Wei Chou. 1995. "Elastic Response and Effect of Transverse Cracking in Woven Fabric Brittle Matrix Composites." *J. Amer. Ceram. Soc.*, 78(3):783–792.
21. R. A. Naik 1995. "Failure Analysis of Woven and Braided Fabric Reinforced Composites." *J. Composite Mater.*, 29(17):2334–2363.
22. R. A. Naik. 1996. "Analysis of Woven and Braided Fabric Reinforced Composites." In R. B. Deo and C. R. Saff, editors, *Composite Materials: Testing and Design (Twelfth Volume), ASTM STP 1274*, pp. 239–263. American Society for Testing and Materials.
23. R. A. Naik. April 7–10, 1997. "Multiaxial Stiffness and Strength Analysis of Woven and Braided Fabric Composites." In *Proceedings of the 38th AIAA/ASME/ASCE/AHS/ASC Structures, Structural Dynamics, and Materials Conference*, Kissimmee, Florida. American Institute of Aeronautics and Astronautics.
24. K. Ranji Vaidyanathan, Jagannathan Sankar, Ajit D. Kelkar, David P. Sinton, and Mark H. Headinger. 1993. "Investigation of Mechanical Properties of Chemically Vapor Infiltrated Ceramic Matrix Composites Under Pure Tension." *Ceram. Engr. Sci. Proc.*, 14(9-10):1016– 1027.
25. K. Ranji Vaidyanathan, Jagannathan Sankar, Ajit D. Kelkar, and Jagdish Narayan. 1994. "Investigation of Mechanical Properties of Chemically Vapor Infiltrated (CVI) Ceramic Matrix Composites." *Ceram. Engr. Sci. Proc.*, 15(4):281–291.
26. L. R. DharanL, D. R. Carroll, S. B. Haug, J. E. Goethe, A. D. Laws, and P. Raj. 1994. "Microcracking Stress and Transverse Properties of Hybrid Ceramic Matrix Composites." *Ceram. Engr. Sci. Proc.*, 15(4):303–308.
27. D. Singh and J. P. Singh. 1992. "Effect of Processing on Strength of Nicalon Fibers in Nicalon Fiber-SiC Matrix Composites." *Ceram. Engr. Sci. Proc.*, 13(7-8):257–266.
28. J. P. Singh, D. Singh, and R. A. Lowden. 1994. "Effect of Fiber Coating on Mechanical Properties of Nicalon Fibers and Nicalon-Fiber/SiC Matrix Composites." *Ceram. Engr. Sci. Proc.*, 15(4): 456–464.
29. S. V. Nair and Yu-Lin Wang. 1992. "Failure Behavior of a 2-D Woven SiC Fiber/SiC Matrix Composite at Ambient and Elevated Temperatures." *Ceram. Engr. Sci. Proc.*, 13(7-8):433–441.
30. Abhisak Chulya, John Z. Gyekenyesi, and John P. Gyekenyesi. 1993. "Failure Mechanisms of 3-D Woven SiC/SiC Composites Under Tensile and Flexural Loading at Room and Elevated Temperatures." *Ceram. Engr. Sci. Proc.*, 13(7-8):420–432.
31. Wayne S. Steffier. 1993. "The Orthotropic Mechanical Behavior of Nicalon Fiber-Reinforced SiC-Matrix Composites." *Ceram. Engr. Sci. Proc.*, 14(9-10):1045–1057.
32. Edgar Lara-Curzio, Mattison K. Ferber, and Richard A. Lowden. 1994. "The Effect of Fiber Coating Thickness on the Interfacial Properties of Continuous Fiber Ceramic Matrix Composite." *Ceram. Engr. Sci. Proc.*, 15(5):989–1000.
33. Dileep Singh and Jitendra P. Singh. 1993. "Effect of High-Temperature Loading on Mechanical Properties of Nicalon Fibers and Nicalon Fiber/SiC Matrix Composites." *Ceram. Engr. Sci. Proc.*, 14(9-10):1153–1164.
34. Michael A. Kmetz, John M. Laliberte, Steven L. Suib, and Francis S. Galasso. 1992. "Synthesis, Characterization and Tensile Strength of CVI C/SiC, SiC/SiC, SiC/B4C and C/B4C Composites." *Ceram. Engr. Sci. Proc.*, 13(9-10):743–751.

35. J. L. Kuhn and P. G. Charalambides. 1997. "Modeling of Plain Weave Fabric Composite Geometry." *In Progress.*
36. Y. P. Qiu and G. J. Weng. 1991. "Elastic Moduli of Thickly Coated Particle and Fiber-Reinforced Composites." *J. Appl. Mech.*, 58:388–398.
37. John L. Bassani. 1991. "Linear Densification and Microcracking in Sintering Compacts." In *Mech. of Mater.*, Volume 12, pp. 119–130. Elsevier Science Publishers B.V.
38. Z. Hashin. 1979. "Analysis of Properties of Fiber Composites with Anisotropic Constituents." *J. Appl. Mech.*, 46:543–550.
39. J. L. Kuhn and P. G. Charalambides. 1997. "Elastic Micro-Fields Plain Weave Fabric Composites under Remote In-Plane Loading." *In Progress.*
40. S. G. Lekhnitskii. 1963. *Theory of Elasticity of an Anisotropic Elastic Body.* Holden-Day, Inc. Translated by P. Fern; Edited by Julius J. Brandstatter.
41. Jonathan L. Kuhn. 1997. *Mechanical Behaviour of Woven Ceramic Matrix Composites.* PhD thesis, The University of Maryland, Baltimore County.
42. Hibbitt, Karlsson & Sorensen, Inc. *ABAQUS.*